Monte-Carlo Analysis of the Influence of the Electrical Component Tolerances on the Behavior of Series-Series- and LCC-Compensated IPT Systems

Francisco Javier López-Alcolea [1], **Javier Vázquez [1]**, **Emilio J. Molina-Martínez [1]**, **Pedro Roncero-Sánchez [1,*]** and **Alfonso Parreño Torres [2]**

[1] Institute of Energy Research and Industrial Applications, University of Castilla-La Mancha, Campus Universitario S/N,13071 Ciudad Real, Spain; FJavier.Lopez@uclm.es (F.J.L.-A.); Javier.Vazquez@uclm.es (J.V.); EmilioJose.Molina@uclm.es (E.J.M.-M.)

[2] Institute of Industrial Development, Castilla-La Mancha Science and Technology Park,Paseo de la Innovación 1, 02006 Albacete, Spain; Alfonso.Parreno@pctclm.com

* Correspondence: Pedro.Roncero@uclm.es

Abstract: The use of compensation networks increases the power transfer capability of inductive power transfer (IPT) systems in the battery charging process of electric vehicles (EVs). Among the proposed topologies, the Series-Series (SS) and the LCC networks are currently in widespread use in wireless battery chargers based on IPT systems. This paper focuses on the study of the behavior of both compensation topologies when they are detuned due to the tolerances of their components. To compare their performances, a Monte-Carlo analysis was carried out using Simulink and MATLAB. The tolerance values, assigned independently to each component, fall within a [−20, 20]% range according to a normal distribution. Histograms and scatter plots were used for comparison purposes. The analysis reveals that the LCC network allows a tighter control over the currents that flow through the magnetic coupler coils. Moreover, it was found that the increments in those currents can be limited to some extent by selecting capacitors featuring low tolerance values in the LCC compensation. Nevertheless, the SS network remains an appropriate choice if size and cost are essential constraints in a given design.

Keywords: series compensation; LCC compensation; electric vehicle; wireless power transfer; inductive power transfer; wireless charging; component tolerances; comparative analysis; Monte-Carlo analysis; simulation model

1. Introduction

The increasing trend in greenhouse gas emissions elucidates the need for a transition to a decarbonized energy system. In this scenario, electric vehicles (EVs) become a clear alternative for internal combustion engine automobiles. Since EV operation does not cause direct emissions, the air pollution from road transport can be significantly reduced if clean energy technologies are adopted. Nevertheless, some aspects concerning the battery pack, such as its charging process, need further investigation.

At first, the EV battery charging process was accomplished by means of conductive chargers. However, the need for a mechanical connection between the transmitter and the receiver increases the electrocution hazard. In these systems, the user needs to touch the transmitter connector. This, in a moist environment or in the case of insulator deterioration, may result in an electrical shock. Wireless Power transfer (WPT) systems diminish remarkably this danger because of the absence of mechanical connectors. In addition, there exist a galvanic isolation between the subsystem installed

in the parking space (ground assembly, *GA*) and the one located in the vehicle (vehicle assembly, *VA*). The acronyms *GA* and *VA* were taken from the standard SAE-J2954 for the recharging of light-duty EVs [1]. These advantages, along with the minor maintenance required, have promoted extensive research in this type of systems.

Near-field WPT systems can be classified according to the electromagnetic phenomenon on which they are based. Capacitive power transfer (CPT) systems use the electric field coupling to transmit power between two conductive surfaces separated by a dielectric medium. Their most common configurations consist of conductive plates with ring and square geometries connected to frequency compensation networks. One or more plates are located at both the transmitter and receiver sides of the system, having as a result two resonant subsystems [2–5].

In inductive power transfer (IPT) systems the conductive surfaces on the transmitter and the receiver sides are replaced by coils. Thus, the magnetic field is the responsible for the power transferred by means of the induction phenomenon. Coil geometries have been widely discussed, being rectangular, circular and double-D coils the most extended configurations [6–8]. Nonetheless, other coil topologies have also been proposed, as the taichi, flux-pipe, cross-shape, hexagonal or the so-called quad D quadrature [9–13].

There exist some advantages in the use of CPT systems. For example, the presence of nearby metal objects results in lower losses since the induced eddy currents are significantly reduced [14]. In addition, they have a lower weight and cost, as well as a smaller magnetic interference with other devices [15]. However, their operation at air-gap distances of about 150 mm results in small capacitances. Therefore, either high operating frequencies (about 1 MHz) or compensation networks with very large inductance values are needed to reach relatively high-power levels [4,16]. Yet another disadvantage is the field shielding. It is harder to attenuate the unwanted electric field emissions than those of the magnetic field. Consequently, CPT systems are more prone to unsafe field emissions than IPT systems [14].

One of the main advantages of inductive over capacitive power transfer is its higher power density. Moreover, high-power transmissions can be achieved at lower operating frequencies with a higher system efficiency. This, along with the easier shielding of the magnetic field, have made IPT technology to stand out as the prevailing choice for WPT charging of EVs batteries [14].

Compensation topologies of IPT systems have been studied in depth, particularly in the grid-to-vehicle (G2V) power transfer direction. Originally, four basic structures were proposed. They are characterized by a compensation capacitor connected, either in series or in parallel, with the coils of the magnetic coupler [17]. Each topology is labeled with two letters. The first one depends on the association of the capacitor with the coil in the *GA* (primary side). When it is connected in series, an S is assigned. On the contrary, if a parallel compensation of the coil is chosen, then a P is used. The same occurs with the second letter, which indicates the type of connection used in the *VA* (secondary side). The Series-Series (SS) compensation stands out among these four basic topologies. Unlike the other three options, its resonance frequency is independent of variations in the magnetic coupling coefficient (k) or in the load connected to the receiver side [18]. However, the transmitted power increases greatly with the misalignment between coils, which may lead to unsafe operation [19].

In order to overcome the disadvantages of the basic compensation topologies, more complex structures have been proposed [20–22]. For example, the use of a parallel compensation in the *VA* requires a large inductor on its corresponding DC side. Its aim is to ensure that the rectifier works under continuous conduction mode [23]. Consequently, the size and the cost of the *VA* electronics are increased. However, if the coil is connected in series with the AC side of the rectifier, the required inductance value significantly reduces. As a result, an LCL network is obtained [23,24].

Variations of this last structure can be found in the literature [25,26]. One of the most accepted topologies is the so-called inductor-capacitor-capacitor (LCC) compensation [27]. The extra coils in an LCL compensation must have the same impedance as the coils in the original magnetic coupler for a perfect tuning condition. In the LCC topology a capacitor is connected in series with the coupler

coil, achieving its partial compensation. As a result, the equivalent impedance is reduced and hence the required self-inductance of the added inductor.

Apart from the double-sided LCC compensation (an LCC network placed both on the *GA* and the *VA* sides), other topologies have been proposed [28,29]. One of the most extended configurations is the LCC-S topology. It consists of an LCC compensation on the *GA* side and a series compensation on the *VA* side. The aim is to reduce both the size and the cost in the *VA* whereas a current-source behavior is still achieved under variations in load and *k* [30–33].

SS and double-sided LCC configurations are currently the most extended topologies, especially when a bidirectional power flow is required. Both configurations exhibit a current-source behavior at the receiver output for a given constant voltage at the transmitter side. Nevertheless, their performance may differ significantly when deviations from the operating point occur. With the aim of establishing the differences and similarities between these two structures, some comparison studies have been reported. In [19], Li et al. analyzed the effects of variations in the coupling coefficient, load and self-inductances of the coils. Zang et al. focused on the distortion that occurs in high-power strongly coupled IPT systems ($k > 0.7$) due to coupled harmonics in [34]. A comparison between SS, parallel-parallel (PP) and LCC topologies was performed by Mohamed et al. in [35]. Finally, Lu et al. evaluated the effects that component tolerances have on the efficiency and output power of an LCC-compensated system in [36].

This paper focuses on the study of the detuned SS- and double-sided LCC-compensated IPT systems because of the tolerances of their network components. First, a mathematical analysis of both tuned topologies is developed to highlight their main characteristics and expected behavior. Secondly, a Monte-Carlo analysis is performed for each topology under the same load and *k* conditions. In each simulation, the tolerances of the compensation components vary within the $[-20, 20]\%$ range according to a normal probability distribution. Histograms and correlation plots are used to perform a multivariate analysis. The aim is to determine to which extent the simultaneous variation in the values of the different components compromise the system performance.

The paper is structured as follows: The mathematical analysis of the two electrical circuit models under consideration is developed in Section 2. Section 3 describes the setup of the corresponding simulation models, while the simulation data are analyzed in Section 4. Finally, the conclusions drawn from this work are discussed in Section 5.

2. Mathematical Modeling of an IPT System with SS and LCC Compensation Networks

With the aim of highlighting the particularities found in both topologies, the mathematical expressions for the SS- and the LCC-compensated magnetic couplers are derived. The analysis is focused on the general scheme of an IPT system depicted in Figure 1. The power transfer from the DC link located at the *GA* to the *VA* is performed by means of an inverter, a compensated magnetic coupler and a rectifier. In turn, the battery pack may either be connected directly to the rectifier output or through an optional DC-DC converter. This last stage, represented in dashed lines, may be added for regulation purposes. If it is ommited, the rectifier DC output voltage, $V_{VA,dc}$, matches the battery voltage, V_{bat}. However, when the DC-DC converter is placed, $V_{VA,dc}$ and V_{bat} are usually different DC voltages.

It is a common practice to replace the rectifier, the optional DC-DC converter and the battery pack with an equivalent resistance [28,30]. This resistor is connected to the *VA* side of the compensated magnetic coupler. As a result, the model simplifies and a linear system that depends on the output voltage of the inverter, V_{GA}, is obtained. However, the expression for the equivalent resistance varies for the SS and LCC topologies. Furthermore, the influence of V_{VA} on the currents flowing through the coils of the magnetic coupler cannot be directly obtained.
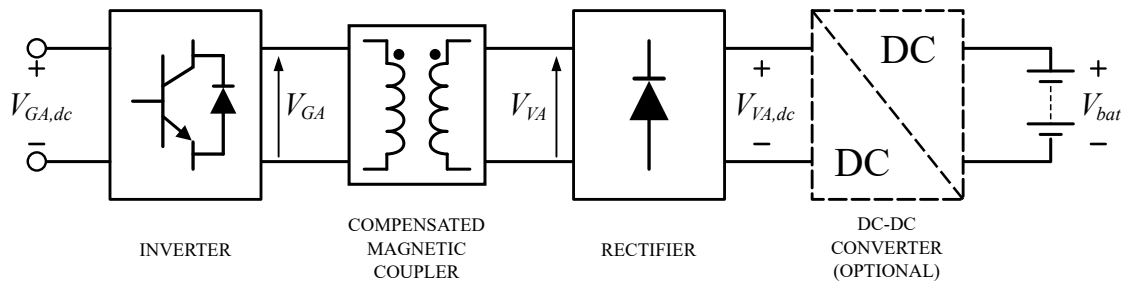
Figure 1. Block diagram of an IPT system featuring an optional DC-DC converter for regulation of the charging process.

To get around this limitation, the mathematical modeling presented in this work follows the analysis adopted in [19,34,37]. It relies on the voltages V_{GA} and V_{VA} in order to describe the behavior of the compensated magnetic coupler. Thus, the use of an equivalent resistance is avoided, and the analysis can be carried out using the original scheme shown in Figure 1. An additional advantage of this approach is that the resulting equations are useful for a bidirectional power flow.

Regardless of the selected procedure, some important assumptions must be taken into account. First, all the non-linear devices in the inverter, the rectifier and the optional converter must behave as ideal components. For example, the switching dynamics and losses in transistors and diodes are neglected. Secondly, the self-inductances in the magnetic coupler must be independent of both the misalignment between coils and the transmitted power. Finally, another important assumption addresses the continuous operation mode of the rectifier. This last assumption is strictly necessary only in the case of using the equivalent resistance. However, if this condition holds also true for the chosen approach, the waveform of the voltage at the rectifier input is square-shaped. In this case, the expression for V_{VA} is simplified, being the amplitude of its *h-th* harmonic [38]:

$$V_{VA,h} = \frac{4V_{VA,dc}}{h\pi}; \ h = 1,2,3\dots \tag{1}$$

The same equation holds true for a square wave at the inverter output, which leads to the following expression for the amplitude of the $h-th$ harmonic of V_{GA}:

$$V_{GA,h} = \frac{4V_{GA,dc}}{h\pi}; \ h = 1,2,3\dots \tag{2}$$

2.1. Mathematical Model for an SS-Compensated Coupler

In order to model the magnetic coupling of the IPT system, the magnetic coupler shown in Figure 1 is substituted by its T equivalent circuit. The resulting electrical model for the SS topology is shown in Figure 2. Here, L_1 and L_2 are the self-inductances of the GA and VA coils, and C_1 and C_2 are the corresponding compensation capacitances. The parasitic resistances of the GA and VA coils (R_1 and R_2, respectively) are included. To express the mutual inductance of the magnetic coupler, the equation $M = k\sqrt{L_1L_2}$ is used.

By applying the superposition theorem, the effect that voltages v_{GA} and v_{VA} have over the currents i_1 and i_2 can be studied from the analysis of two separated circuits. In each case, either v_{GA} or v_{VA} is taken as a short circuit, remaining the other unaltered. Consequently, two systems of differential equations in the time domain can be obtained. Thus, the contribution of v_{GA} and v_{VA} to the currents

i_1 and i_2 can be calculated independently. Taking v_{VA} as a short circuit, the equations that express the influence of v_{GA} on i_1 and i_2 are:

$$\begin{cases} v_{GA} = \dfrac{1}{C_1}\displaystyle\int i_{1,GA}\,dt + (L_1 - M)\dfrac{di_{1,GA}}{dt} + M\dfrac{d}{dt}(i_{1,GA} - i_{2,GA}) + R_1 i_{1,GA} \\[2mm] M\dfrac{d}{dt}(i_{1,GA} - i_{2,GA}) = \dfrac{1}{C_2}\displaystyle\int i_{2,GA}\,dt + (L_2 - M)\dfrac{di_{2,GA}}{dt} + R_2 i_{2,GA} \end{cases} \tag{3}$$
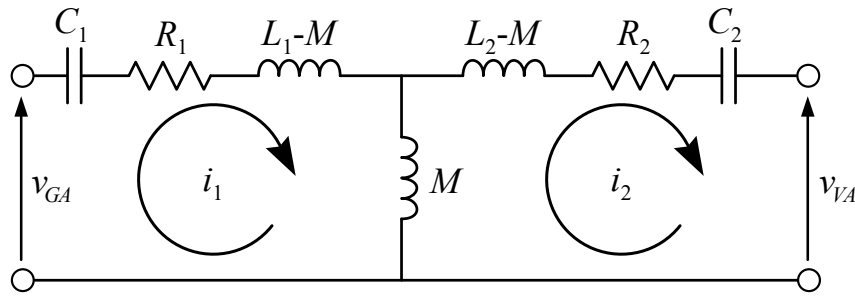

Figure 2. Equivalent circuit of an SS-compensated coupler.

where the subscript GA in the currents denotes the dependency of the currents on v_{GA}. Likewise, the influence that v_{VA} has on i_1 and i_2 can be obtained from the following equations:

$$\begin{cases} v_{VA} + \dfrac{1}{C_2}\displaystyle\int i_{2,VA}\,dt + (L_2 - M)\dfrac{di_{2,VA}}{dt} + M\dfrac{d}{dt}(i_{2,VA} - i_{1,VA}) + R_2 i_{2,VA} = 0 \\[2mm] M\dfrac{d}{dt}(i_{2,VA} - i_{1,VA}) = \dfrac{1}{C_1}\displaystyle\int i_{1,VA}\,dt + (L_1 - M)\dfrac{di_{1,VA}}{dt} + R_1 i_{1,VA} \end{cases} \tag{4}$$

where the lower-case letters are used to express instantaneous voltages and currents. The subscript VA shows the dependency of the currents on v_{VA}.

The corresponding frequency-dependent equations can be obtained by applying the Laplace transform to their time-domain counterparts given by (3) and (4). Solving the equations in the phasor domain for the two currents yields the following solutions:

$$\vec{I_1} = \overline{Y}_{1,GA}\vec{V}_{GA} + \overline{Y}_{1,VA}\vec{V}_{VA} = \frac{\overline{Z}_2}{\overline{Z}_1\overline{Z}_2 + \omega^2 M^2}\vec{V}_{GA} - \frac{j\omega M}{\overline{Z}_1\overline{Z}_2 + \omega^2 M^2}\vec{V}_{VA} \tag{5}$$

$$\vec{I_2} = \overline{Y}_{2,GA}\vec{V}_{GA} + \overline{Y}_{2,VA}\vec{V}_{VA} = \frac{j\omega M}{\overline{Z}_1\overline{Z}_2 + \omega^2 M^2}\vec{V}_{GA} - \frac{\overline{Z}_1}{\overline{Z}_1\overline{Z}_2 + \omega^2 M^2}\vec{V}_{VA} \tag{6}$$

where upper-case letters express the frequency-dependent terms. Voltages and currents are related through the admittances $\overline{Y}$ which, in turn, can be expressed in terms of the impedances $\overline{Z}_1$ and $\overline{Z}_2$:

$$\overline{Z}_1 = j\omega L_1 + \frac{1}{j\omega C_1} + R_1$$

$$\overline{Z}_2 = j\omega L_2 + \frac{1}{j\omega C_2} + R_2 \tag{7}$$

When the imaginary parts of $\overline{Z}_1$ and $\overline{Z}_2$ become zero, the reactances of the coils are compensated by the capacitors and the circuit is perfectly tuned. This condition leads to the definition of the resonant frequency, $\omega_r = 2\pi f_r$:

$$\omega_r = \frac{1}{\sqrt{L_1 C_1}} = \frac{1}{\sqrt{L_2 C_2}} \tag{8}$$

By analyzing (6), it can be seen that I_2 depends on the load because of the voltage V_{VA}. Therefore, the current-source behavior is, in principle, not achieved. However, the terms $\overline{Z}_1$ and $\overline{Z}_2$ become negligible at the resonant frequency and the dependency on V_{VA} virtually vanishes. For this reason, the desired current-source behavior at the rectifier input is a reasonable approximation for an SS compensation topology under resonance conditions. In addition, if the parasitic resistances R_1 and R_2 are neglected, the output current I_2 on the secondary side will be totally load-independent.

In that case, if all the harmonic components apart from the fundamental one are neglected (i.e., $h = 1$ and $\omega = \omega_r$), the expressions (5) and (6) simplify to:

$$\vec{I}_1 = -\frac{j}{\omega_r M}\vec{V}_{VA,1} = -\frac{j}{\omega_r k\sqrt{L_1 L_2}}\vec{V}_{VA,1} \tag{9}$$

$$\vec{I}_2 = \frac{j}{\omega_r M}\vec{V}_{GA,1} = \frac{j}{\omega_r k\sqrt{L_1 L_2}}\vec{V}_{GA,1} \tag{10}$$

Thus, if the power dissipated in the system is neglected, the apparent power of the IPT system, S, can be written as:

$$S = \frac{1}{2}|\vec{I}_1|\cdot|\vec{V}_{GA,1}| = \frac{1}{2}|\vec{I}_2|\cdot|\vec{V}_{VA,1}| = \frac{1}{\omega_r k\sqrt{L_1 L_2}}V_{VA,1}V_{GA,1} \tag{11}$$

A notorious disadvantage that can be derived from Equations (9) and (10) is the dependency of both I_1 and I_2 on k. According to previous works [39–42], if some degree of misalignment exists or if the air gap between both coils is wider than expected, the value of k decreases. Consequently, there is an increase in both currents, which may lead to an unsafe operation. This is a serious drawback that arises when designing an SS-compensated IPT system, as it must be able to operate safely even in a worst-case scenario.

However, there are some notorious advantages in the use of an SS compensation. First, the design of C_1 and C_2 is straightforward, as the resonance condition only depends on L_1, L_2, and the desired resonant frequency. Secondly, since the coils are compensated in series, a voltage source inverter (VSI) can be connected directly to the compensated magnetic coupler. Therefore, no additional inductors are needed, unlike for a parallel connection [43]. As a result, the number of compensation elements is kept to a minimum. This leads to a lower cost and size of both the *GA* and *VA* sides in a bidirectional system.

2.2. Mathematical Model for an LCC-Compensated Coupler

The equivalent circuit of an LCC-compensated coupler is shown in Figure 3. Here, C_1 and C_2 correspond to the partial compensations of the coils L_1 and L_2. There exist four added compensation components, labeled as C_{f1}, C_{f2}, L_{f1} and L_{f2} that are not used in the SS topology. Again, the parasitic resistances of the coils are taken into account in the model, including those corresponding to L_{f1} and L_{f2}.

With the aim of simplifying the mathematical modeling of the LCC-compensated system, only the mutual inductance between the coils L_1 and L_2 is considered. Thus, the remaining mutual inductances between the pairs of coils L_1-L_{f1}, L_2-L_{f2} and L_{f1}-L_{f2} are neglected. This assumption is valid in systems where there exists a proper isolation of the magnetic field in the coils L_{f1} and L_{f2}. For example, by reducing their leakage flux to a minimum with the use of a magnetic core and placing both coils sufficiently far from the magnetic coupler. Furthermore, this holds also true when L_{f1} and L_{f2} are integrated into the magnetic coupler so that the coupled flux in those coils is negligible, as in [44,45].

This time, the application of the superposition theorem results in the following system of differential equations for $V_{VA} = 0$:

$$
\begin{cases}
v_{GA} = L_{f1}\dfrac{di_{f1,GA}}{dt} + R_{f1}i_{f1,GA} + \dfrac{1}{C_{f1}}\displaystyle\int (i_{f1,GA} - i_{1,GA})\,dt \\[2mm]
\dfrac{1}{C_{f1}}\displaystyle\int (i_{f1,GA} - i_{1,GA})\,dt = \dfrac{1}{C_1}\displaystyle\int i_{1,GA}\,dt + R_1 i_{1,GA} + (L_1 - M)\dfrac{di_{1,GA}}{dt} + M\dfrac{d(i_{1,GA} - i_{2,GA})}{dt} \\[2mm]
M\dfrac{d(i_{1,GA} - i_{2,GA})}{dt} = (L_2 - M)\dfrac{di_{2,GA}}{dt} + R_2 i_{2,GA} + \dfrac{1}{C_2}\displaystyle\int i_{2,GA}\,dt + \dfrac{1}{C_{f2}}\displaystyle\int (i_{2,GA} - i_{f2,GA})\,dt \\[2mm]
\dfrac{1}{C_{f2}}\displaystyle\int (i_{2,GA} - i_{f2,GA})\,dt = R_{f2}i_{f2,GA} + L_{f2}\dfrac{di_{f2,GA}}{dt}
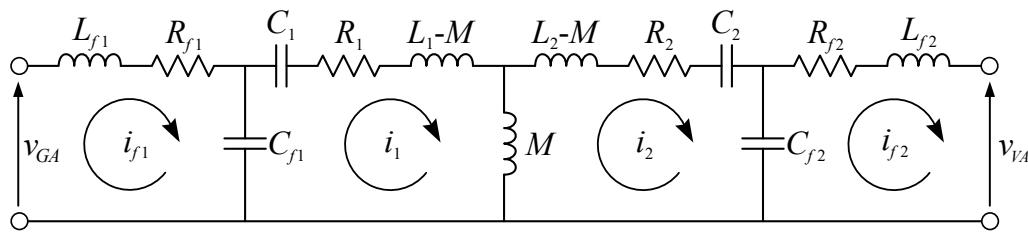\end{cases}
\tag{12}
$$

Figure 3. Equivalent circuit of an LCC-compensated coupler.

In turn, the case $V_{GA} = 0$ gives the second set of equations:

$$
\begin{cases}
0 = L_{f1}\dfrac{di_{f1,VA}}{dt} + R_{f1}i_{f1,VA} + \dfrac{1}{C_{f1}}\displaystyle\int (i_{f1,VA} - i_{1,VA})\,dt \\[2mm]
\dfrac{1}{C_{f1}}\displaystyle\int (i_{f1,VA} - i_{1,VA})\,dt = \dfrac{1}{C_1}\displaystyle\int i_{1,VA}\,dt + R_1 i_{1,VA} + (L_1 - M)\dfrac{di_{1,VA}}{dt} + M\dfrac{d(i_{1,VA} - i_{2,VA})}{dt} \\[2mm]
M\dfrac{d(i_{1,VA} - i_{2,VA})}{dt} = (L_2 - M)\dfrac{di_{2,VA}}{dt} + R_2 i_{2,VA} + \dfrac{1}{C_2}\displaystyle\int i_{2,VA}\,dt + \dfrac{1}{C_{f2}}\displaystyle\int (i_{2,VA} - i_{f2,VA})\,dt \\[2mm]
\dfrac{1}{C_{f2}}\displaystyle\int (i_{2,VA} - i_{f2,VA})\,dt = R_{f2}i_{f2,VA} + L_{f2}\dfrac{di_{f2,VA}}{dt} + v_{VA}
\end{cases}
\tag{13}
$$

As stated previously in the mathematical analysis of the SS compensation, the subscripts GA and VA express the dependency of the currents on v_{GA} and v_{VA} in both systems of linear equations.

The translation of the expressions (12) and (13) into the frequency domain results in an equivalent set of equations that are noticeably more tedious and complex to solve than in the previous case. This time there are eight admittances to calculate that consist of high-order polynomials, either in the numerator or the denominator. It is convenient, therefore, to simplify the general equations by operating the IPT system at the resonance frequency and neglecting the parasitic resistances.

The tuning condition of the LCC topology is more complicated than in the case of the SS topology. This time, the system will be tuned at the resonant frequency ($\omega = \omega_r$) if the following expression is fulfilled [16]:

$$
\omega_r = \frac{1}{\sqrt{L_{f1}C_{f1}}} = \frac{1}{\sqrt{L_{f2}C_{f2}}} = \frac{1}{\sqrt{(L_1 - L_{f1})C_1}} = \frac{1}{\sqrt{(L_2 - L_{f2})C_2}}
\tag{14}
$$

Under these assumptions, the currents at the *GA* and *VA* sides are given by [16]:

$$\vec{I}_{f1} = \frac{k\sqrt{L_1 L_2}}{j\omega_r L_{f1} L_{f2}} \vec{V}_{VA,1} ; \quad \vec{I}_{f2} = \frac{k\sqrt{L_1 L_2}}{j\omega_r L_{f1} L_{f2}} \vec{V}_{GA,1} \tag{15}$$

$$\vec{I}_1 = \frac{1}{j\omega_r L_{f1}} \vec{V}_{GA,1} ; \quad \vec{I}_2 = -\frac{1}{j\omega_r L_{f2}} \vec{V}_{VA,1} \tag{16}$$

Thus, the apparent power at the input, S_1, and output, S_2, of the compensated coupler can be expressed as:

$$S_1 = \frac{1}{2} |\vec{I}_{f1}| \cdot |\vec{V}_{GA,1}| = \frac{k\sqrt{L_1 L_2}}{2\omega_r L_{f1} L_{f2}} V_{VA,1} V_{GA,1} \tag{17}$$

$$S_2 = \frac{1}{2} |\vec{I}_{f2}| \cdot |\vec{V}_{VA,1}| = \frac{k\sqrt{L_1 L_2}}{2\omega_r L_{f1} L_{f2}} V_{GA,1} V_{VA,1} \tag{18}$$

where, again, S_1 and S_2 are equal due to the ideal conditions under which they were derived.

It is apparent that the LCC compensation results in a more complex IPT system, which is a disadvantage when compared to the SS compensation. However, the following three specific issues make the LCC topology outperform its SS counterpart in an IPT system. First, when designing the magnetic coupler, its nominal operating current is established. Since I_1 and I_2 are independent of the load and the coupling coefficient, as stated in (16), a fully tuned LCC-compensated IPT system helps to keep both currents within a safe range [27,46]. Therefore, the LCC compensation provides a higher protection against saturation and deterioration of the magnetic coupler caused by excessively high currents. Moreover, it also prevents the saturation of magnetic couplers featuring ferrite cores, which are currently in widespread use in IPT prototypes designed for powering EVs.

The second significant advantage is the direct dependency of I_{f1} and I_{f2} with k, as follows from (15). As stated previously, if misalignment occurs or the air gap is increased, the value of k decreases. Consequently, both I_{f1} and I_{f2} decrease as well. The same occurs with the apparent power at both the inverter output and the rectifier input, as shown in (17) and (18).

Finally, it can be seen from (11) that the output power of an SS-compensated IPT system depends on V_{VA} and V_{GA}, on M and on ω_r. However, the output power of an LCC-compensated IPT system depends not only on those parameters but also on L_{f1} and L_{f2}, as stated previously in (18). This means that there exist two extra parameters in an LCC compensation that need to be designed, which is an interesting feature. The mutual inductance depends on both the misalignment and the air gap between coils, while the operating frequency range is determined by the standard SAE-J2954 [19]. Thus, both parameters cannot be used to adjust the power transferred in the design stage. With the double-sided LCC compensation, the added coils L_{f1} and L_{f2} can be used for this purpose. Therefore, the nominal voltages on the *VA* and *GA* sides can be determined from other constraints, such as the battery voltage.

3. Set-Up of the Simulation Model

The aim of this work is to evaluate the behavior of the SS and LCC topologies when the tolerance values are the only parameters that fluctuate. For this purpose, a sensitivity analysis was performed. The derivation of mathematical expressions results in a cumbersome work since the IPT system works out of the resonance condition. In addition, if the main assumptions are not fulfilled (e.g., negligible power losses and parasitic resistances), the simplified equations previously derived are no longer valid. To overcome these limitations, a simulation model was developed for each topology by using the Simscape Toolbox in Simulink. The same tools were used to run the models.

The selected variables to perform the analysis correspond to the RMS currents and the average power that flow through the compensation networks. For this purpose, the RMS values of the currents I_1 and I_2 (along with I_{f1} and I_{f2} for the LCC topology) were selected. Regarding the power estimations,

the average active and apparent power at the input and output terminals of the compensated magnetic coupler were used. The average input and output powers were calculated using the first, third and fifth harmonic components throughout the analysis.

3.1. Design of the Compensation Parameters and Nominal Operating Point

In order to compare the SS and the LCC topologies, both simulated systems are tuned to work under the same resonant frequency and nominal apparent power. Furthermore, the coupling parameters L_1, L_2 and k are kept constant so that both networks compensate an identical magnetic coupler. The same occurs with the DC voltages $V_{GA,dc}$ and $V_{VA,dc}$, which are calculated by means of (1), (2) and (11), leading to the following expression:

$$V_{GA,dc} = V_{VA,dc} = \sqrt{\frac{\pi^2}{8} S_n \omega_r k \sqrt{L_1 L_2}} \tag{19}$$

For the sake of clarity, the values assigned to the parameters that remain unaltered in both compensated systems are shown in Table 1. The first (and easiest) system to tune corresponds to the SS topology. For this network, the capacitances are selected to make the system resonate at $\omega_r = 2\pi f_r$ by means of the Equation (8):

$$C_1 = \frac{1}{\omega_r^2 L_1} ; \quad C_2 = \frac{1}{\omega_r^2 L_2} \tag{20}$$

Table 1. Shared parameters between the SS and LCC compensations.

Parameter	Value	Parameter	Value
L_1 (µH)	146.8	S_n (kW)	1
L_2 (µH)	144.5	$V_{GA,dc}$ (V)	160
k	0.25	$V_{VA,dc}$ (V)	160
f_r (kHz)	87		

On the other hand, the tuning process for the LCC compensation follows the steps outlined in [27]. As a result, the following expressions for the values of the components are obtained:

$$L_{f1} = \sqrt{\frac{k V_{GA,1} V_{VA,1}}{\omega_r S_n}} L_1 ; \quad L_{f2} = \sqrt{\frac{k V_{GA,1} V_{VA,1}}{\omega_r S_n}} L_2 \tag{21}$$

$$C_{f1} = \frac{1}{\omega_r^2 L_{f1}} ; \quad C_{f2} = \frac{1}{\omega_r^2 L_{f2}} \tag{22}$$

$$C_1 = \frac{1}{\omega_r^2 (L_1 - L_{f1})} ; \quad C_2 = \frac{1}{\omega_r^2 (L_2 - L_{f2})} \tag{23}$$

The application of both design procedures results in the compensation parameters shown in Table 2. With the aim of simulating a realistic system, the parasitic resistances in each coil were included. In addition, the capacitances are accurate to a single decimal place, since the precision needed for a perfect tuning is hard to achieve in an experimental arrangement.

Through the use of Tables 1 and 2, the nominal operating points (shown in Table 3) can be established. As can be seen, the apparent power achieved with both compensated systems differs slightly from the target value of 1 kW set for S_n on Table 1. Moreover, the efficiency of the SS-compensated magnetic coupler is larger than the one obtained with the LCC compensation. According to [47], if L_{f1}, $L_{f2} \approx M$ it follows that the efficiencies of both systems must be similar, provided the IPT systems are ideal. However, this does not hold exactly true in our case, owing to the influence of the parasitic resistances and the rounding of the compensation parameters. Thus,

these two factors explain both the observed deviations from the expected S_n and the lower efficiency of the LCC-compensated IPT system.

Table 2. Unshared compensation parameters between the LCC and SS topologies.

SS Compensation		LCC Compensation			
Parameter	Value	Parameter	Value	Parameter	Value
C_1 (nF)	22.8	L_{f1} (μH)	37.3	L_{f2} (μH)	37
C_2 (nF)	23.2	C_1 (nF)	30.6	C_2 (nF)	31.1
R_1 (Ω)	0.2	C_{f1} (nF)	89.7	C_{f2} (nF)	90.4
R_2 (Ω)	0.2	R_1 (Ω)	0.2	R_2 (Ω)	0.2
		R_{f1} (Ω)	0.2	R_{f2} (Ω)	0.2

Table 3. Nominal operating points for the simulated LCC- and SS-compensated systems.

SS Compensation				LCC Compensation			
Variable	Value	Variable	Value	Variable	Value	Variable	Value
S_1 (VA)	1086.8	$I_{1,RMS}$ (A)	7.31	S_1 (VA)	1074.6	$I_{1,RMS}$ (A)	7.03
S_2 (VA)	1062.2	$I_{2,RMS}$ (A)	7.15	S_2 (VA)	1001.6	$I_{2,RMS}$ (A)	7.23
P_1 (W)	1076.6			P_1 (W)	1035.5	$I_{f1,RMS}$ (A)	7.30
P_2 (W)	1054.8			P_2 (W)	993.65	$I_{f2,RMS}$ (A)	7.01
η (%)	97.97			η (%)	95.96		

3.2. Assignment of Tolerances for the Multivariate Analysis

A key setting in the simulation models is the assignment of electrical component tolerances. In both studies, it is supposed that the values of all the components range from a minimum of 80% to a maximum of 120% of its nominal values. Hence, a tolerance range of ±20% is set for each component.

In the multivariate analysis, the assigned tolerances follow a normal distribution characterized by a mean $\mu = 0$ and a standard deviation $\sigma = 6.6$. This value for σ guarantees that 99.7% of the values of the ideal population are within the $[-19.7, 19.7]$% range. Hence, limiting the minimum and maximum values of the generated sample to -20% and 20%, respectively, is a reasonable assumption. For each component, a different set of pseudo-random values was assigned by means of the MATLAB function *randn* with an initial sample size of 1500 values per component.

After simulating both systems, some of the obtained histograms had heavy tails. Consequently, the number of simulations was increased to 150,000 points for each topology. To illustrate this, Figure 4 shows a histogram and a scatter plot of the same variable for the two cases. Both histograms were normalized by using the probability density function (PDF) so that they can be compared avoiding the distortion caused by the sample size. The bigger data set gives a better match between the histogram and the fitted distribution, especially for the heavy tails. Moreover, the scatter plots show that the number of simulation points that fall near the 20% tolerance range is small for the data set of 1500 points. By increasing the number of simulations to 150,000, this is corrected.

The histograms obtained for the tolerances assigned in the SS-compensated system take the form shown in Figure 5. Here, the number of occurrences (hereafter called *frequency*) is shown and the fitted normal distributions are superimposed. In order to calculate the bin width of each histogram, the Sturges' rule is applied to a specified range. Taking w_{hist} as the range width, the bin width of the histogram can be calculated as [48]:

$$\text{Bin width} = \frac{w_{hist}}{1 + log_2(n)} \tag{24}$$

where n corresponds to the number of observations located within the selected range.

For the histograms shown in Figure 5, the $[-20, 20]$% range was selected. As a result, a bin width of 2.2% is obtained for the 150,000 simulations in the sample. The use of the Freedman-Diaconis

rule was also evaluated. However, the resulting bin widths were excessively narrow, not only for the above-mentioned histograms but for others used later in this work.
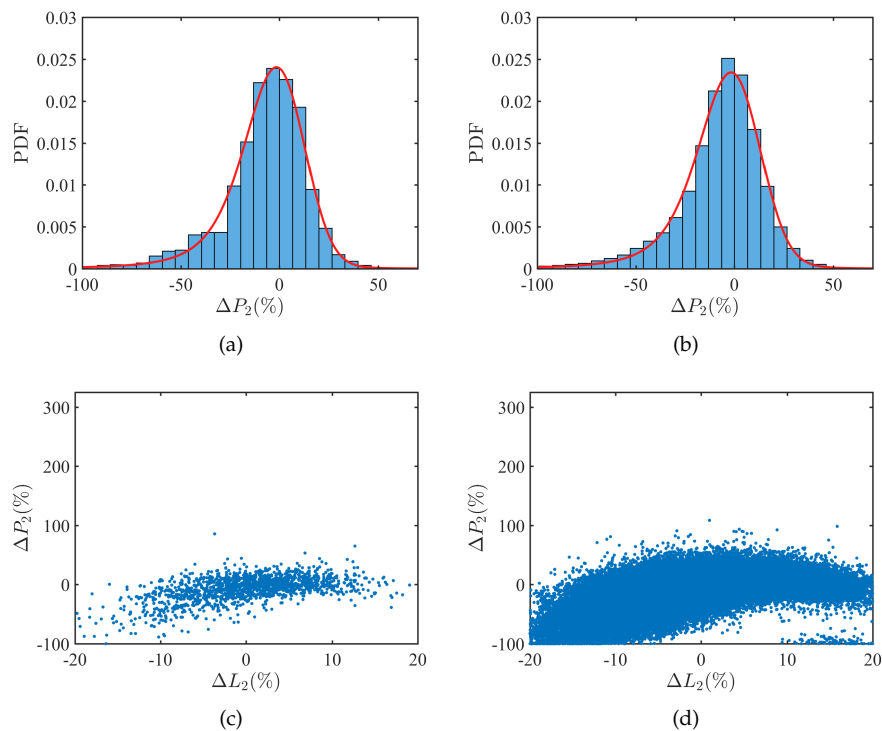

Figure 4. Histograms and scatter plots used to illustrate the effect of augmenting the size of the data set. In subfigures (**a**,**c**) 1500 simulations were used, while subfigures (**b**,**d**) correspond to a data set of 150,000 points.

As can be seen, the $\hat{\mu}$ and $\hat{\sigma}$ values obtained for each case in Figure 5 are close to their respective initial settings. In addition, the histograms follow appropriately a normal distribution, hence the population is large enough. Moreover, it can be seen from $\hat{\mu}$ and $\hat{\sigma}$ that each population slightly differs from the others. This procedure was also followed for the LCC compensation parameters and the results are very similar. Consequently (and for the sake of brevity), their histograms are not shown.
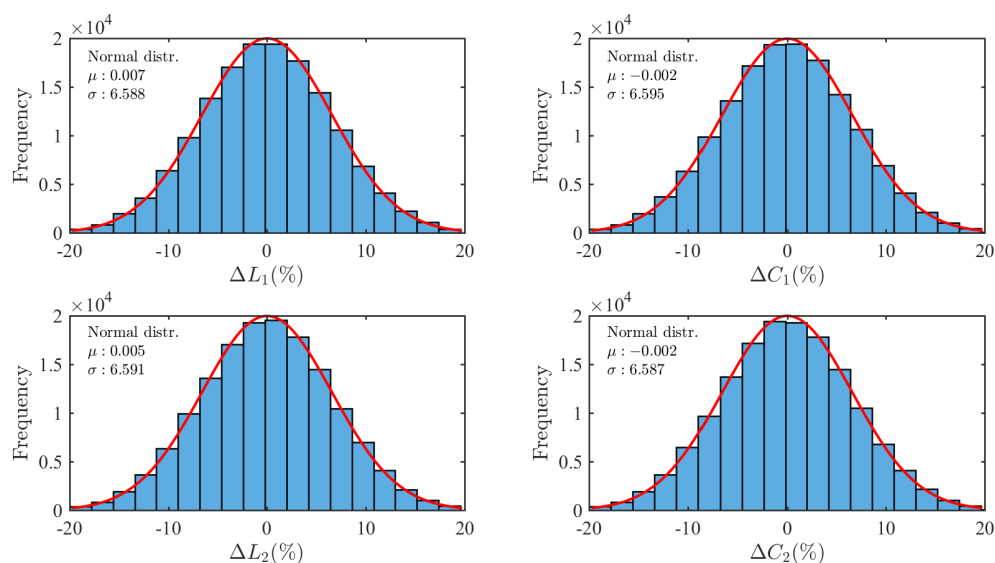
Figure 5. Histograms of the tolerances assigned to each parameter during the Monte-Carlo simulation of the SS-compensated system.

4. Analysis of the Monte-Carlo Simulations

The multivariate analysis focuses on the comparison between the SS and the LCC compensations when the component values vary simultaneously. For this purpose, two complementary approaches are applied.

First, the evaluation of the trends observed for the currents, the active and the apparent power (hereafter defined together as *variables*) is performed through the use of normalized histograms. The normalization used in this work corresponds to an estimate of the PDF of the sample. To calculate the bin width, the range where the fitted PDF cannot be ignored is selected for each variable. The empirical PDFs are fitted using stable distributions, unless otherwise indicated. This distribution is appropriate for the analysis since the deviations from the nominal operating point are caused by the normally distributed variations of the tolerances. The distribution fitting of the histograms was carried out by using the MATLAB function *fitdist*.

Secondly, scatter plots are represented. The primary purpose of this approach is to find out whether or not there exist a strong correlation between the tolerances of each component and any of the variables. If such correlations exist, the equation for a straight line is obtained along with the Pearson and the determination (or R-squared, R^2) coefficients. The Pearson correlation coefficient helps to determine how accurate the hypothesis of a linear dependency between both variables is. On the other hand, the R^2 accounts for the percentage of the variation of the sample that can be explained by the model.

With the aim of avoiding the use of units, both the variables and component quantities are expressed as deviations from its nominal values. In doing so, the analyzed data do not correspond to absolute values but to relative increments instead, avoiding misinterpretations derived from scale effects.

4.1. SS-Compensated IPT System

The histograms that result from the simulation of the SS-compensated system are shown in Figure 6. The x-axis stretches from -100% to 70% for all the variables under consideration because most of the simulated data fit within that range in both topologies. However, a few fall beyond these limits. The IPT system is compensated with resonant networks, thus it is inherently sensitive to the deviations of the components. Hence, the operation off resonance may result in either a significant increase or decrease of the measured variables. For example, the maximum deviations observed during the Monte-Carlo simulations correspond to $\Delta P_2 = -99.99\%$ and $\Delta I_{1,RMS} = 320.65\%$ for the SS topology. Regarding the LCC compensation, $\Delta I_{f2,RMS} = -99.99\%$ and $\Delta I_{f1,RMS} = 189.21\%$ are the maximum values observed. These deviations are in agreement with those reported in [16], where the output power vary from 0 W to more than 11.5 kW for a 5.7 kW LCC-compensated IPT system in a $[-10, 10]\%$ tolerance range. For the sake of accuracy, it should be pointed out that none of the data points that fall outside the chosen range are disregarded in the computational work. Their exclusion is only effective in the visualization of the histograms.

For a better understanding of the distribution profiles obtained from the simulations, the range $[-20, 20]\%$, is shadowed in the histograms. It corresponds to the boundaries previously set for the variation of the components. Please note that outside these boundaries, the GA and VA sides respond quite differently. On the GA side, the simulated data for $I_{1,RMS}$ and S_1 largely exceed the 20% upper boundary, resulting in positively skewed distribution profiles in both cases. On the contrary, both $I_{2,RMS}$ and S_2 on the VA side appear well below the -20% lower boundary. A similar divergent trend is observed when comparing P_1, which has certain deviations near -100%, with S_1, where most of the simulated data exhibit positive percentage deviations. The observed distribution profiles are in agreement with the increase in reactive power produced by the detuned networks. Thus, the power transfer capability of the IPT system is reduced. For this reason, both the RMS current $I_{2,RMS}$, the active power P_2 and the apparent power S_2 on the VA side decrease as a consequence of the corresponding fall undergone by P_1.
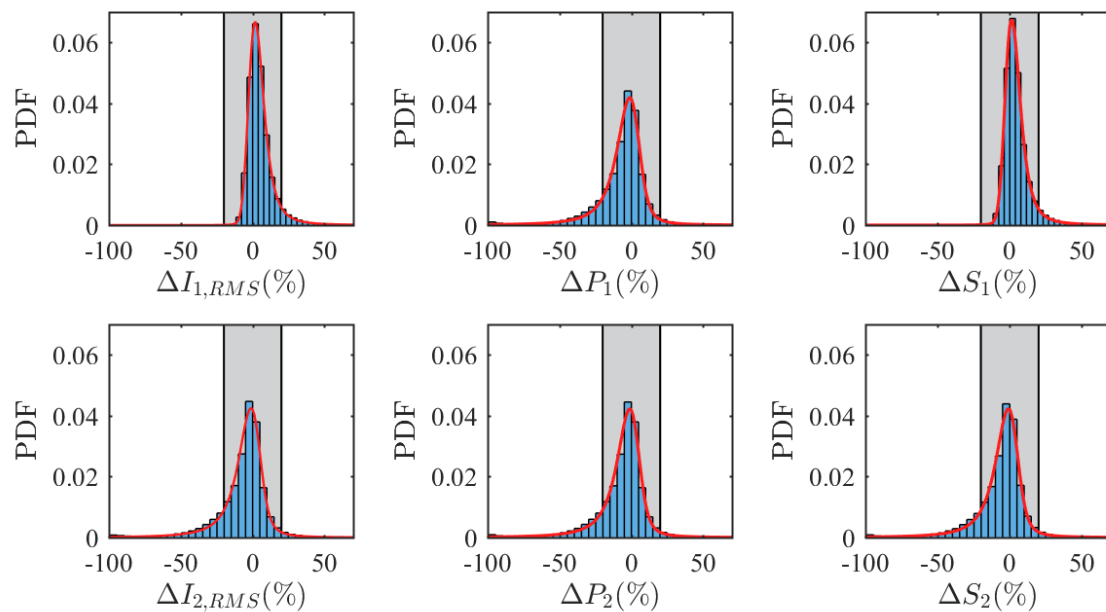
Figure 6. Normalized histograms of the measurements for the SS compensation.

If the area of the bars covered by the $[-20, 20]\%$ range is compared with the whole surface represented in the histogram, the empirical probability for that particular range is obtained. This statistical parameter is shown in Table 4. As can be seen, the empirical probabilities for $I_{1,RMS}$ and S_1 are remarkably larger. This is entirely consistent with the distribution profiles observed in the histograms, where a relevant percentage of the simulations are located near the nominal operating point for $I_{1,RMS}$ and S_1.

Table 4. Estimated empirical probability of the variables under study for the SS-compensated system

Variable	Empirical Probability (%)	Variable	Empirical Probability (%)
$\Delta I_{1,RMS}$	93.29	ΔP_1	81.79
$\Delta I_{2,RMS}$	81.98	ΔP_2	81.81
		ΔS_1	93.63
		ΔS_2	82.04

The x-axis in the scatter plots ranges from -20% to 20% while the y-axis is set up so that all the simulated data points are included. For the sake of clarity, all the graphics obtained for each pair component-variable are shown in Appendix A. Only one dispersion graph per variable is shown in Figure 7, except for the efficiency. As can be seen, there is not a strong correlation for most of the represented variables. The lack of such correlations in the multivariate analysis is not surprising since the simultaneous variation of two or more components influence the samples involved in each variable. However, this result is not necessarily expected in the univariate case, where strong correlations may occur in certain cases. To illustrate this, Figure 8 shows the variations of $I_{2,RMS}$, P_2 and S_2 when all parameters are kept constant except C_1. For this analysis, the tolerances vary from -20% to 20% in steps of 0.4%. As there is no other variation that affects the sample in neither of the three cases, the correlations between those variables and ΔC_1 can be clearly seen. However, such correlations are not so evident in the multivariate plots shown in Figure 7.
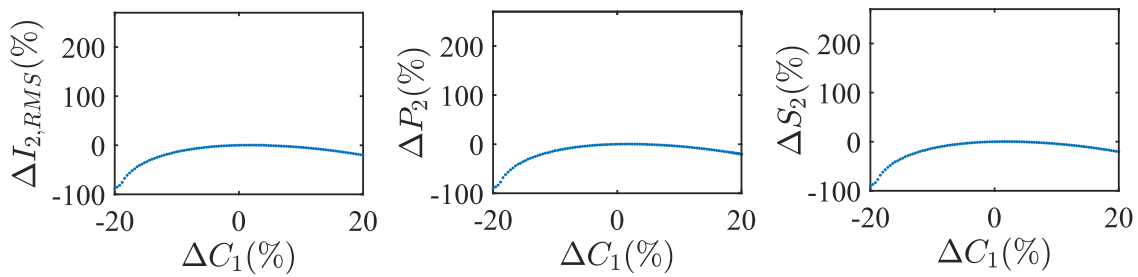
Figure 8. Variations in $I_{2,RMS}$, P_2 and S_2 when C_1 is the only parameter that varies within its tolerance range.
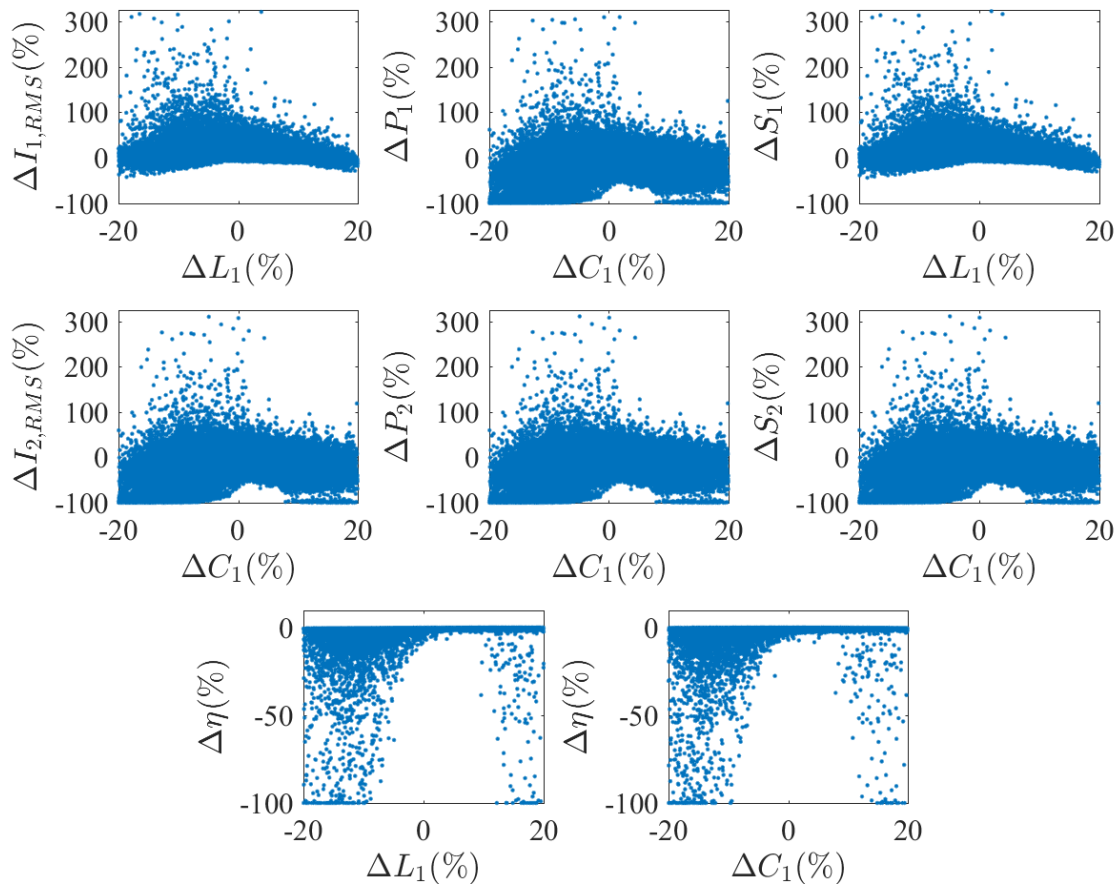

Figure 7. Selection of scatter plots for the variables under study in the SS-compensated system when all the compensation components vary simultaneously within their respective tolerance ranges. Each plot represents the degree of correlation found between a simulated variable and a single component.

By inspecting the dispersion graphs for η shown in Figure 7, it is apparent that small tolerances may lead to a reduction in the variations observed. However, those tolerances must be significantly small to keep such deviations within reasonable limits. Unfortunately, this is difficult to achieve for the coupler coils, since the tolerance range of commercial coils is usually large.

On the other hand, it should be noted that the scatter plots for P_1 and P_2 and their corresponding correlations are quite similar to each other. However, owing to the increase undergone by the reactive power under detuning conditions, this does not hold true for S_1 and S_2.

4.2. LCC-Compensated System

The histograms for the variables of the LCC-compensated system are shown in Figure 9. Here, the x- and y-axes boundaries are the same as in the SS compensation analysis so that the distribution profiles obtained in both cases can be compared without distortion. Again, some data points are not represented in the histograms despite being considered in the fitting.

When comparing the histograms shown in Figure 9 with those in Figure 6, it can be concluded that the distribution profiles of the LCC network are more symmetrical. Aiming at a better interpretation of these distribution profiles, the obtained values for the empirical probabilities are collected in Table 5. In general terms, a decrease in the empirical probabilities is observed except for the RMS values of the currents I_1 and I_2. In fact, when the empirical probabilities of both currents are calculated within the broader range of $[-30,30]$%, their values increase to nearly 100% for the LCC compensation. The resulting probabilities are 99.20% for $I_{1,RMS}$ and 99.95% for $I_{2,RMS}$, whereas in the case of the SS topology the calculations result in 96.99% and 90.25%, respectively. This means that despite the higher dispersion observed, the LCC compensation maintains the RMS currents at both sides of the magnetic coupler nearer its nominal values.

Please note that in this case the resulting distribution profiles for the active and apparent power are not so different from each other as they turn out to be with the SS compensation. The operation of the IPT system off resonance necessarily increases the reactive power regardless of the compensation network used. However, it is apparent from the power histograms that the power transfer capability is compromised to a lesser extent if an LCC instead of an SS compensation is used. This is consistent with the conclusions drawn in [19].
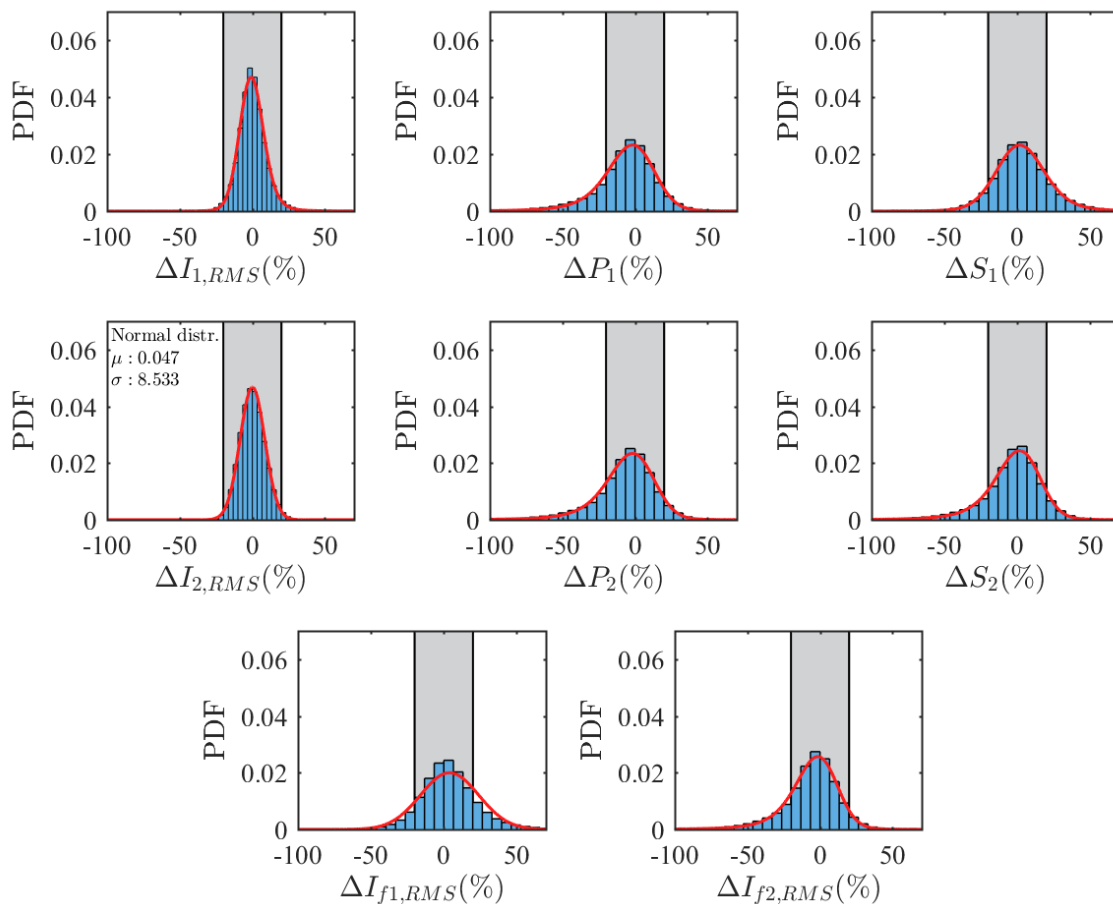

Figure 9. Normalized histograms of the measurements for the LCC compensation.

Table 5. Estimated empirical probability of the variables under study for the LCC-compensated system

Variable	Empirical Probability (%)	Variable	Empirical Probability (%)
$\Delta I_{1,RMS}$	95.46	ΔP_1	72.99
$\Delta I_{2,RMS}$	98.02	ΔP_2	73.18
$\Delta I_{f1,RMS}$	74.15	ΔS_1	73.98
$\Delta I_{f1,RMS}$	76.31	ΔS_2	75.19

The entire set of scatter plots obtained for the LCC-compensated system are collected in Appendix B, whereas one dispersion graph per variable is shown in Figure 10. As can be seen, there is a noticeable correlation between the pair $C_{f1} - I_{1,RMS}$ and also between the pair $C_{f2} - I_{2,RMS}$. Consequently, the variations on $I_{1,RMS}$ and $I_{2,RMS}$ can be reduced simply by selecting capacitors C_{f1} and C_{f2} characterized by tolerance figures as small as possible. To illustrate this, a comparative example is shown in Table 6. It compares the maximum deviations found in the entire data set with those obtained for a subset where the tolerance range for C_{f1} and C_{f2} is $[-5, 5]\%$. From the 150,000 points in the sample, $44,777$ points meet this requirement.
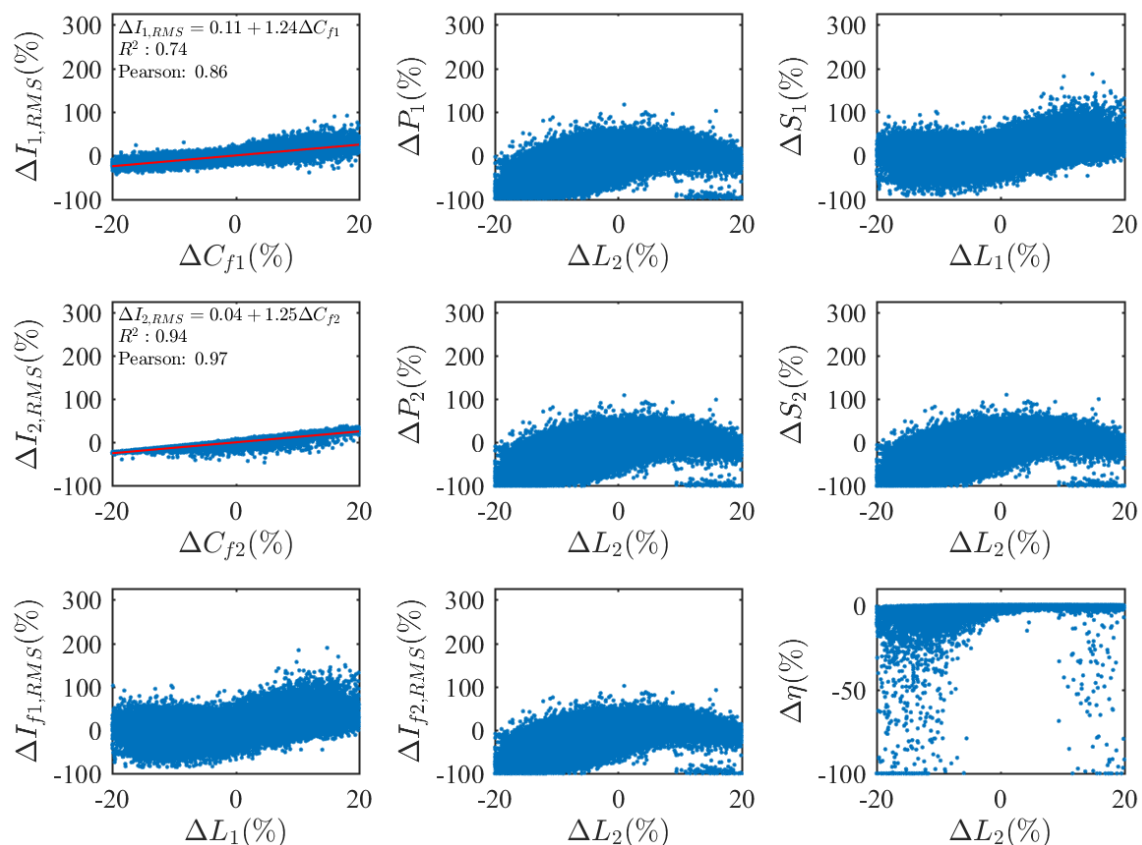
Figure 10. Selection of scatter plots for the variables under study in the LCC-compensated system when all the compensation components vary simultaneously within their respective tolerance ranges. Each plot represents the degree of correlation found between a simulated variable and a single component.

Upon comparing the results, it is apparent that a significant reduction in the tolerance interval contributes to narrow down the shifts from their nominal values undergone by the currents. In particular, it helps to prevent significant increases in both currents. Obviously, the number of possible combinations with non-zero tolerances in a real system is virtually infinite. Thus, the deviations shown in Table 6 must be taken with caution. Nevertheless, this is an interesting result of practical interest

in the design of IPT systems. The adjustment of the tolerances of the capacitors C_{f1} and C_{f2} gives a way of controlling, at least to a certain extent, the potentially large increments in $I_{1,RMS}$ and $I_{2,RMS}$.

Table 6. Maximum deviations obtained for $I_{1,RMS}$ and $I_{2,RMS}$ under different tolerance values assigned to C_{f1} and C_{f2}.

Variable	$\Delta C_{f1}, \Delta C_{f2}$ (%)	Max. Negative Deviation (%)	Max. Positive Deviation (%)
$I_{1,RMS}$	±20.00	−42.95	91.25
	±5.00	−27.08	36.73
$I_{2,RMS}$	±20.00	−46.22	37.95
	±5.00	−37.45	13.41

5. Conclusions

In this work, the influence that the tolerances of the compensation components have on both an SS- and a double-sided LCC-compensated IPT system was investigated. For this purpose, the variations in the currents, the power transferred, and the efficiency were evaluated for both topologies. The main characteristics of each compensation topology are first highlighted for the case of a fully tuned system through a mathematical analysis. Secondly, the expected behavior of the two detuned networks is compared through a Monte-Carlo analysis.

The mathematical analysis shows that both topologies have a current-source behavior at the output of the *VA* side for a fully tuned system, provided the RMS voltage at the VSI output is constant. Under these conditions, the lower cost and reduced complexity of the SS-compensated IPT system are valuable advantages. However, the output power is inversely related with the coupling coefficient k in the SS topology, which may result in an unsafe operation when misalignment occurs. This drawback can be solved by using an LCC compensation instead, for which output power and k are directly proportional. Moreover, the RMS currents on both sides of the magnetic coupler remain constant against variations in either the load or k. This fact makes the LCC network stand out as the preferred choice when a high uncertainty in any of the two parameters is expected.

The Monte-Carlo analysis reveals that the SS compensation leads to an overall smaller deviation from its nominal operating point against the variation of the compensation components. However, this does not hold true for the currents through the coils of the magnetic coupler. For $I_{1,RMS}$ and $I_{2,RMS}$, the LCC topology shows a better capability to maintain both currents within the $[-20, 20]\%$ range. Moreover, the LCC-compensated IPT system shows a smaller increase in the reactive power. Thus, a higher power transfer capability under detuning conditions is obtained. In addition, correlations between C_{f1} and $I_{1,RMS}$ and also between C_{f2} and $I_{2,RMS}$ arose from the scatter plots corresponding to the LCC compensation. Hence, the increase in both currents can be limited, at least to a certain extent, simply by selecting capacitors with low tolerance values for C_{f1} and C_{f2}. This is arguably a result of practical interest in the design of IPT systems.

In conclusion, despite its higher complexity and cost, the LCC compensation guarantees a safer operation when there is a high degree of uncertainty in k. In addition, it has a higher power transfer capability and provides a tighter control of the RMS currents on both coils in the magnetic coupler. Nevertheless, the SS network is still an appropriate choice for those IPT systems where size and weight must be optimized.

Author Contributions: Conceptualization, F.J.L.-A. and J.V.; methodology, F.J.L.-A. and P.R.-S.; software, F.J.L.-A.; validation, J.V., P.R.-S. and A.P.T.; formal analysis, F.J.L.-A., J.V. and E.J.M.-M.; investigation, J.V. and P.R.-S.; resources, P.R.-S. and J.V.; writing—original draft preparation, F.J.L.-A. and J.V.; writing—review and editing, F.J.L.-A., J.V. and P.R.-S.; visualization, F.J.L.-A. and E.J.M.-M.; supervision, P.R.-S. and A.P.T.; project administration, P.R.-S.; funding acquisition, P.R.-S. All authors have read and agreed to the published version of the manuscript.

Conflicts of Interest: The authors declare no conflict of interest. The funders had no role in the design of the study; in the collection, analyses, or interpretation of data; in the writing of the manuscript, or in the decision to publish the results.

Abbreviations

The following abbreviations are used in this manuscript:

EV	Electric Vehicle
WPT	Wireless Power Transfer
GA	Ground Assembly
VA	Vehicle Assembly
CPT	Capacitive Power Transfer
IPT	Inductive Power Transfer
G2V	Grid-to-Vehicle
SS	Series-Series
k	Coupling coefficient
PP	Parallel-Parallel
LCC	Inductor-Capacitor-Capacitor
VSI	Voltage Source Inverter
PDF	Probability Density Function

Appendix A. Scatter Plots for the SS-Compensated System
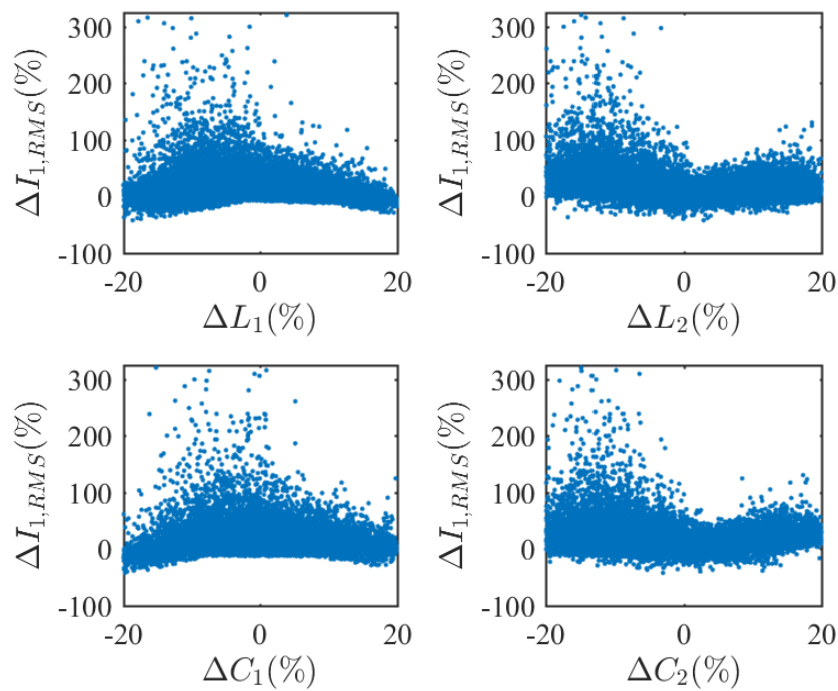
Figure A1. Scatter plots showing the variation of $I_{1,RMS}$ for an SS-compensated system.
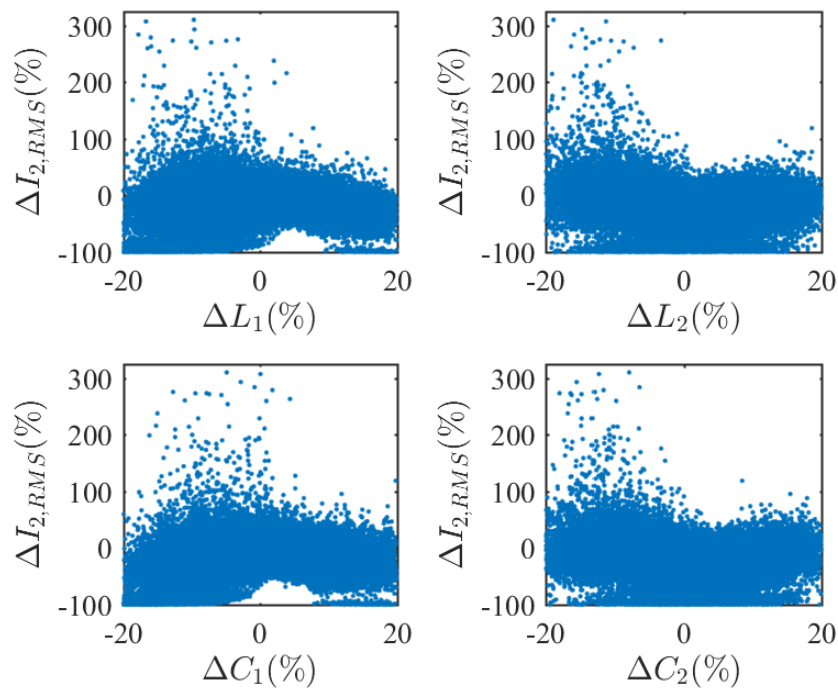
Figure A2. Scatter plots showing the variation of $I_{2,RMS}$ for an SS-compensated system.
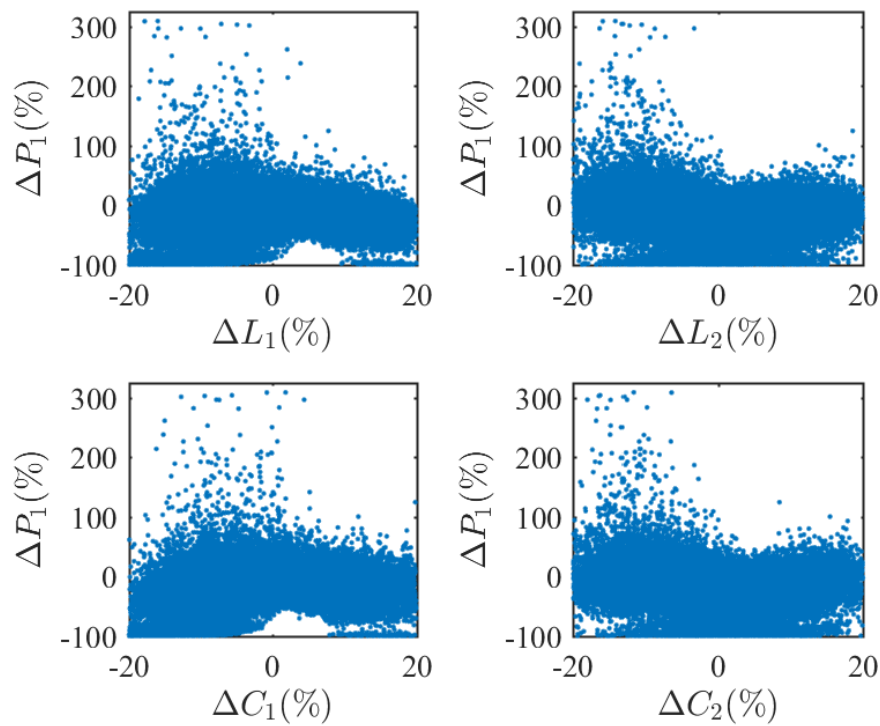
Figure A3. Scatter plots showing the variation of P_1 for an SS-compensated system.
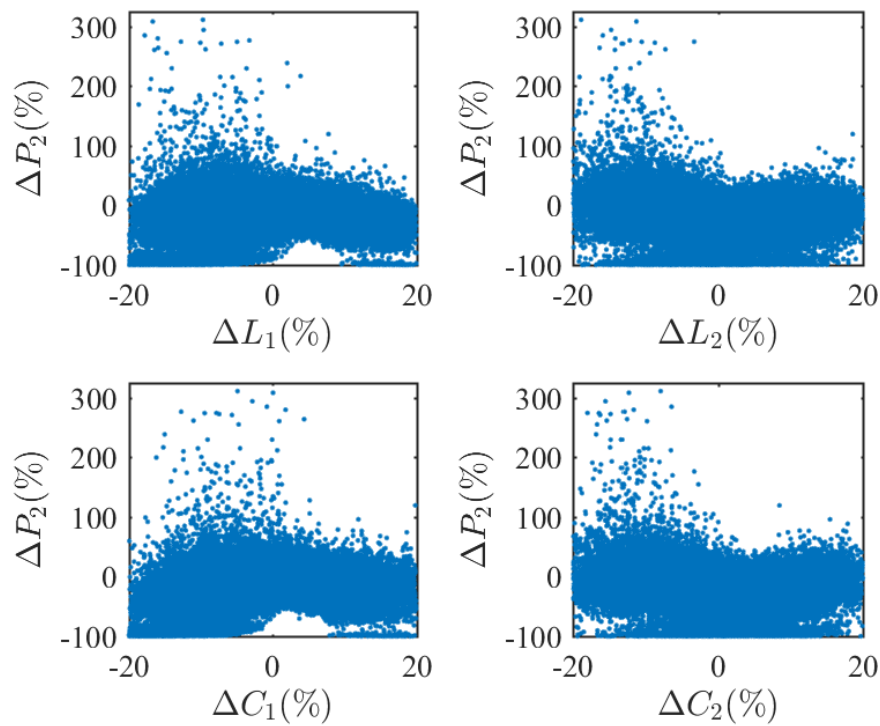
Figure A4. Scatter plots showing the variation of P_2 for an SS-compensated system.
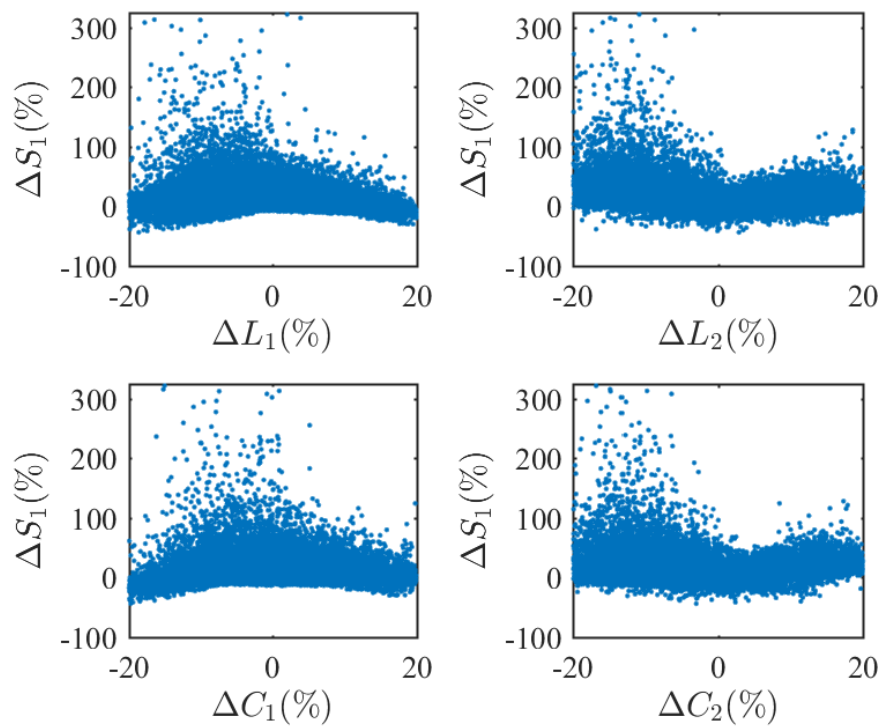
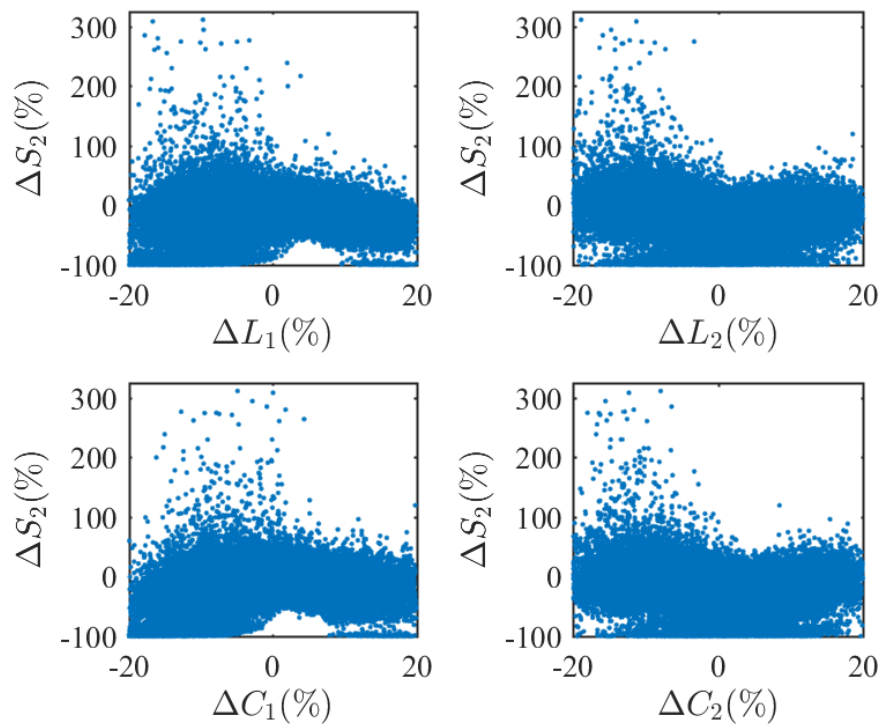**Figure A5.** Scatter plots showing the variation of S_1 for an SS-compensated system.

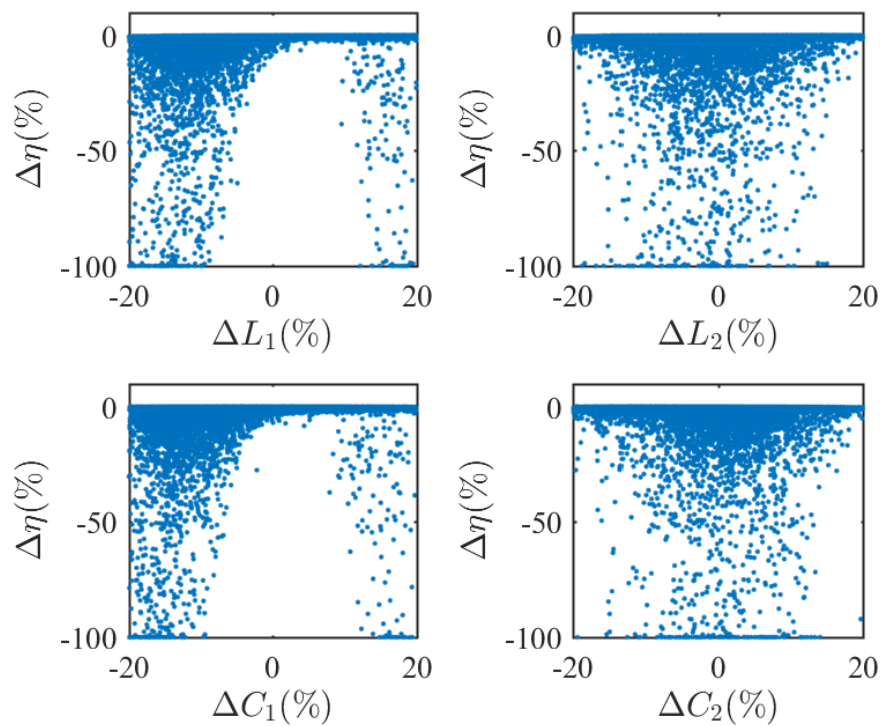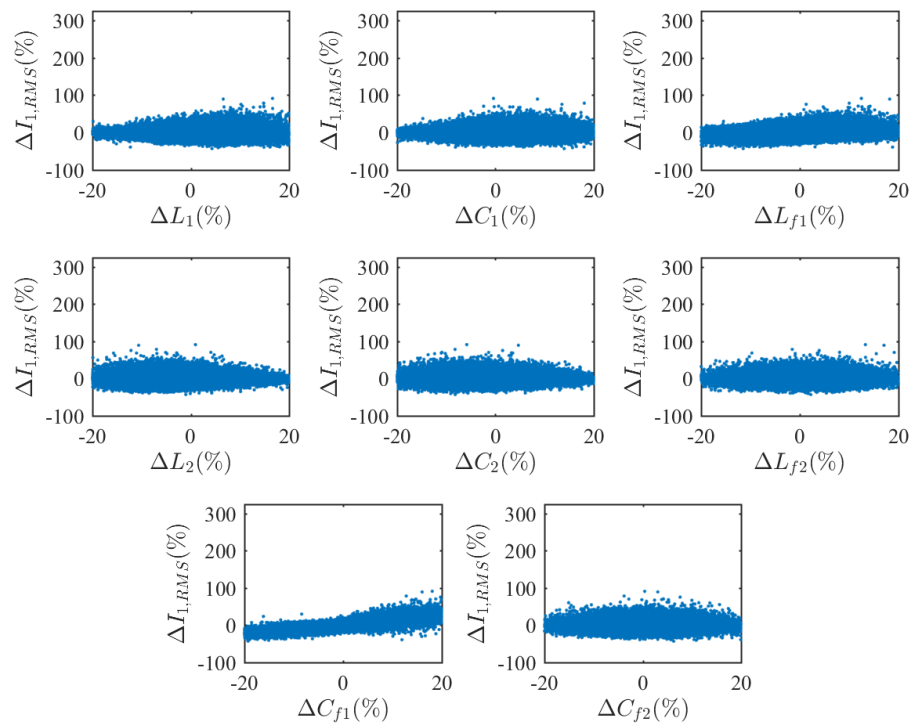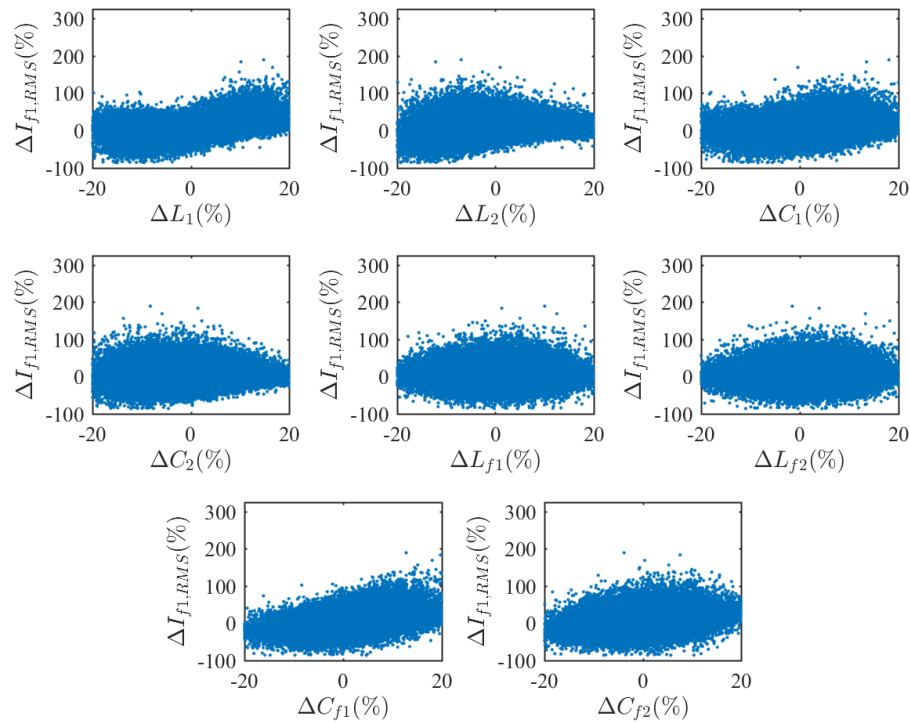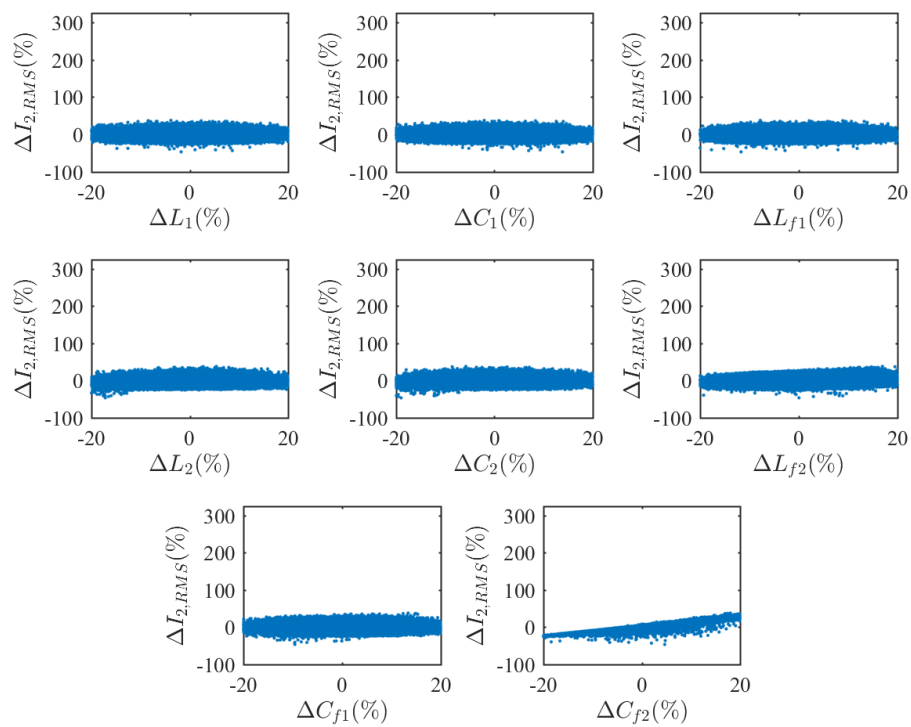**Figure A6.** Scatter plots showing the variation of S_2 for an SS-compensated system.

Figure A7. Scatter plots showing the variation of η for an SS-compensated system.

Appendix B. Scatter Plots for the LCC-Compensated System

Figure A8. Scatter plots showing the variation of $I_{1,RMS}$ for an LCC-compensated system.

Figure A9. Scatter plots showing the variation of $I_{f1,RMS}$ for an LCC-compensated system.

Figure A10. Scatter plots showing the variation of $I_{2,RMS}$ for an LCC-compensated system.
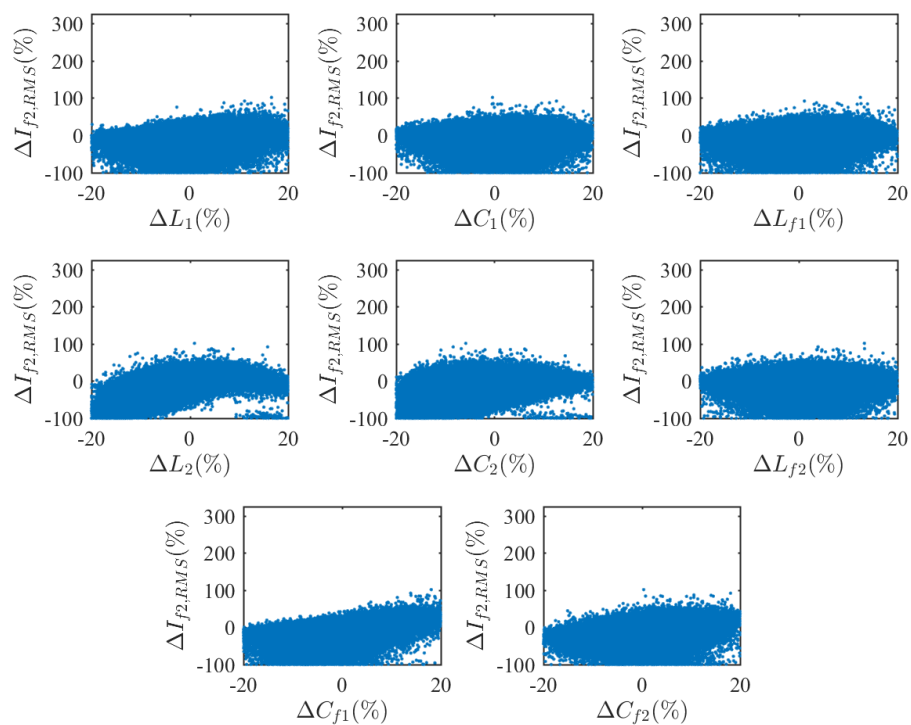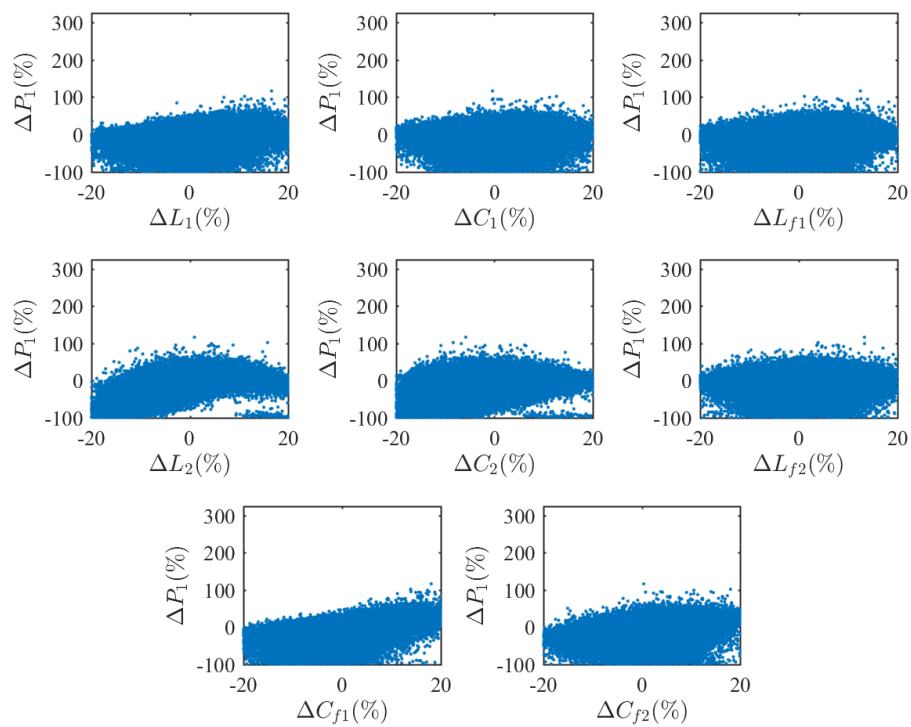

Figure A11. Scatter plots showing the variation of $I_{f2,RMS}$ for an LCC-compensated system.

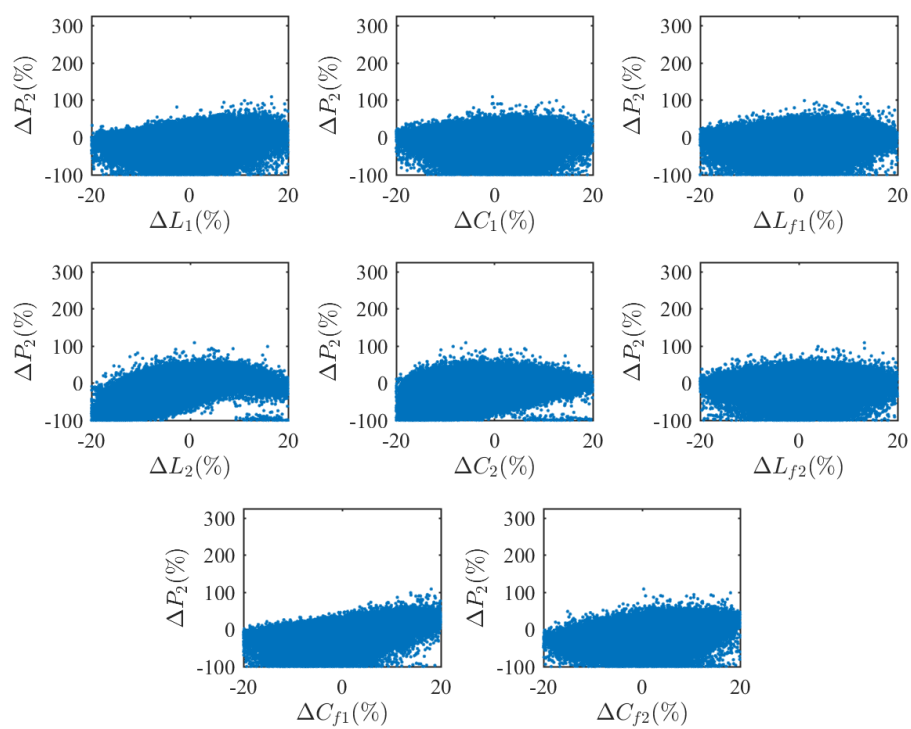**Figure A12.** Scatter plots showing the variation of P_1 for an LCC-compensated system.

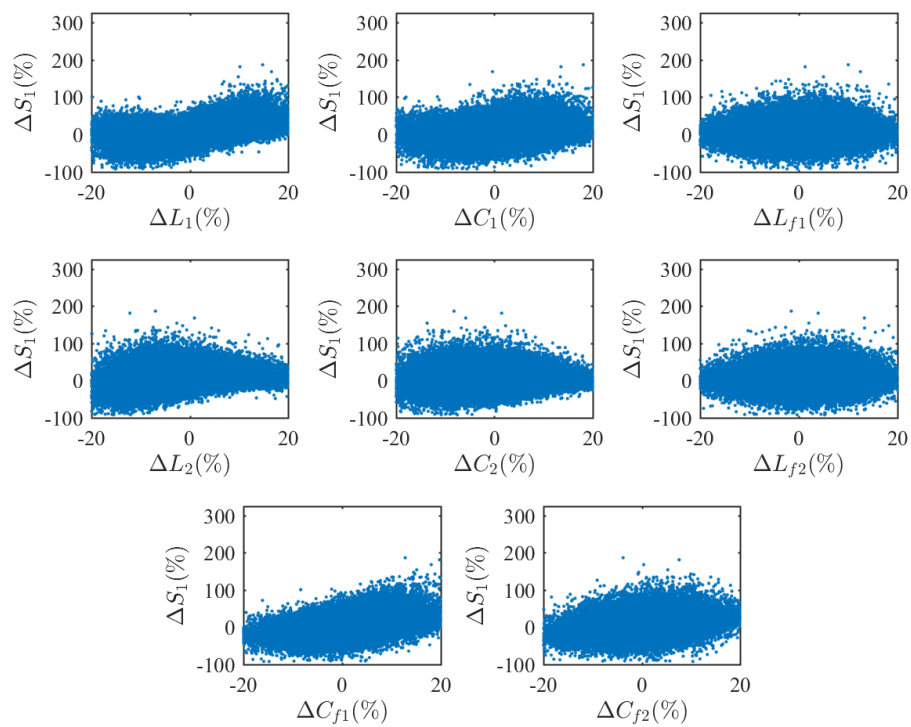**Figure A13.** Scatter plots showing the variation of P_2 for an LCC-compensated system.

Figure A14. Scatter plots showing the variation of S_1 for an LCC-compensated system.
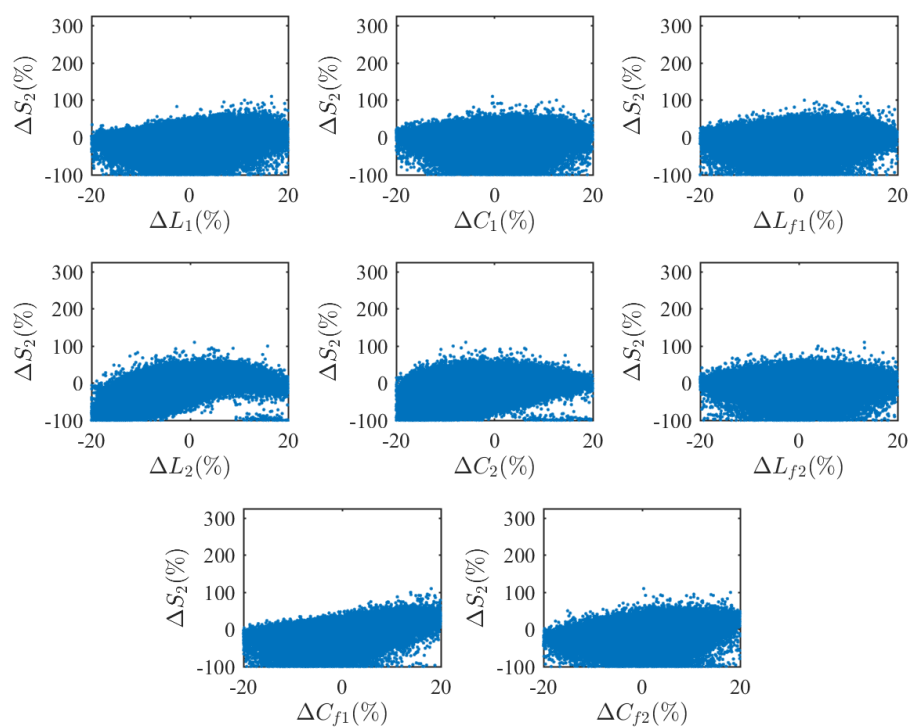

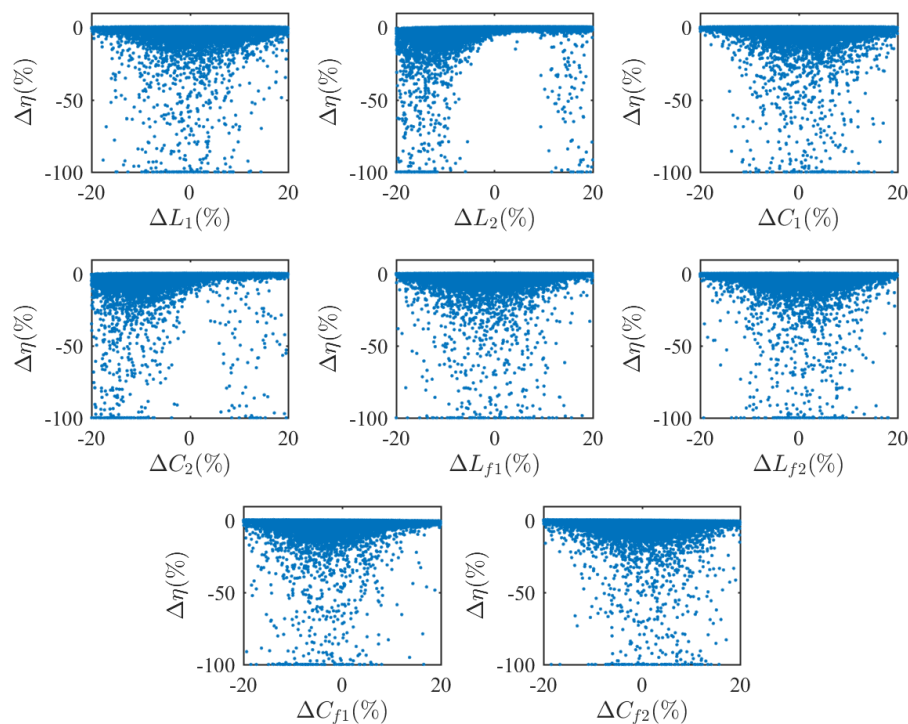**Figure A15.** Scatter plots showing the variation of S_2 for an LCC-compensated system.

Figure A16. Scatter plots showing the variation of *η* for an LCC-compensated system.

References

1. Standard, S. Wireless Power Transfer for Light-Duty Plug-In/Electric Vehicles and Alignment Methodology. In *SAE J2954 TIR*; SAE: Warrendale, PA, USA, 2019. [CrossRef]

2. Al-Saadi, M.; Al-Gizi, A.; Ahmed, S.; Al-Chlaihawi, S.; Craciunescu, A. Analysis of Charge Plate Configurations in Unipolar Capacitive Power Transfer System for the Electric Vehicles Batteries Charging. *Procedia Manuf.* **2019**, *32*, 418–425. [CrossRef]

3. Zhu, Q.; Zou, L.J.; Su, M.; Hu, A.P. Four-plate capacitive power transfer system with different grounding connections. *Int. J. Electr. Power Energy Syst.* **2020**, *115*, 105494. [CrossRef]

4. Lu, F.; Zhang, H.; Hofmann, H.; Mi, C.C. An Inductive and Capacitive Combined Wireless Power Transfer System WithLC-Compensated Topology. *IEEE Trans. Power Electron.* **2016**, *31*, 8471–8482. [CrossRef]

5. Regensburger, B.; Kumar, A.; Sinha, S.; Doubleday, K.; Pervaiz, S.; Popovic, Z.; Afridi, K. High-performance large air-gap capacitive wireless power transfer system for electric vehicle charging. In Proceedings of the 2017 IEEE Transportation Electrification Conference and Expo (ITEC), Chicago, IL, USA, 22–24 June 2017; pp. 638–643. [CrossRef]

6. Bosshard, R.; Iruretagoyena, U.; Kolar, J.W. Comprehensive Evaluation of Rectangular and Double-D Coil Geometry for 50 kW/85 kHz IPT System. *IEEE J. Emerg. Sel. Top. Power Electron.* **2016**, *4*, 1406–1415. [CrossRef]

7. Zhang, W.; White, J.C.; Abraham, A.M.; Mi, C.C. Loosely Coupled Transformer Structure and Interoperability Study for EV Wireless Charging Systems. *IEEE Trans. Power Electron.* **2015**, *30*, 6356–6367. [CrossRef]

8. Deng, J.; Li, W.; Nguyen, T.D.; Li, S.; Mi, C.C. Compact and Efficient Bipolar Coupler for Wireless Power Chargers: Design and Analysis. *IEEE Trans. Power Electron.* **2015**, *30*, 6130–6140. [CrossRef]

9. Li, Y.; Zhao, J.; Yang, Q.; Liu, L.; Ma, J.; Zhang, X. A Novel Coil With High Misalignment Tolerance for Wireless Power Transfer. *IEEE Trans. Magn.* **2019**, *55*, 1–4. [CrossRef]

10. Olukotun, B.; Partridge, J.; Bucknall, R. Finite Element Modeling and Analysis of High Power, Low-loss Flux-Pipe Resonant Coils for Static Bidirectional Wireless Power Transfer. *Energies* **2019**, *12*, 3534. [CrossRef]

11. Sis, S.A.; Orta, E. A Cross-Shape Coil Structure for Use in Wireless Power Applications. *Energies* **2018**, *11*, 1094. [CrossRef]

12. Castillo-Zamora, I.U.; Huynh, P.S.; Vincent, D.; Perez-Pinal, F.J.; Rodriguez-Licea, M.A.; Williamson, S. Hexagonal Geometry Coil for a WPT High Power Fast Charging Application. *IEEE Trans. Transp. Electrif.* **2019**, *5*, 946–956. [CrossRef]

13. Kalwar, K.A.; Mekhilef, S.; Seyedmahmoudian, M.; Horan, B. Coil Design for High Misalignment Tolerant Inductive Power Transfer System for EV Charging. *Energies* **2016**, *9*, 937. [CrossRef]

14. Lu, F.; Zhang, H.; Mi, C. A Review on the Recent Development of Capacitive Wireless Power Transfer Technology. *Energies* **2017**, *10*, 1752. [CrossRef]

15. Yusop, Y.; Saat, S.; Husin, H.; Nguang, S.K.; Hindustan, I. Analysis of Class-E LC Capacitive Power Transfer System. *Energy Procedia* **2016**, *100*, 287–290. [CrossRef]

16. Lu, F.; Zhang, H.; Hofmann, H.; Mi, C. A Double-SidedLCLC-Compensated Capacitive Power Transfer System for Electric Vehicle Charging. *IEEE Trans. Power Electron.* **2015**, *30*, 6011–6014. [CrossRef]

17. Machura, P.; Li, Q. A critical review on wireless charging for electric vehicles. *Renew. Sustain. Energy Rev.* **2019**, *104*, 209–234. [CrossRef]

18. Shevchenko, V.; Husev, O.; Strzelecki, R.; Pakhaliuk, B.; Poliakov, N.; Strzelecka, N. Compensation Topologies in IPT Systems: Standards, Requirements, Classification, Analysis, Comparison and Application. *IEEE Access* **2019**, *7*, 120559–120580. [CrossRef]

19. Li, W.; Zhao, H.; Deng, J.; Li, S.; Mi, C.C. Comparison Study on SS and Double-Sided LCC Compensation Topologies for EV/PHEV Wireless Chargers. *IEEE Trans. Veh. Technol.* **2016**, *65*, 4429–4439. [CrossRef]

20. Villa, J.L.; Sallan, J.; Sanz Osorio, J.F.; Llombart, A. High-Misalignment Tolerant Compensation Topology For ICPT Systems. *IEEE Trans. Ind. Electron.* **2012**, *59*, 945–951. [CrossRef]

21. Samanta, S.; Rathore, A.K. A New Current-Fed CLC Transmitter and LC Receiver Topology for Inductive Wireless Power Transfer Application: Analysis, Design, and Experimental Results. *IEEE Trans. Transp. Electrif.* **2015**, *1*, 357–368. [CrossRef]

22. Hou, J.; Chen, Q.; Wong, S.; Tse, C.K.; Ruan, X. Analysis and Control of Series/Series-Parallel Compensated Resonant Converter for Contactless Power Transfer. *IEEE J. Emerg. Sel. Top. Power Electron.* **2015**, *3*, 124–136. [CrossRef]

23. Keeling, N.A.; Covic, G.A.; Boys, J.T. A Unity-Power-Factor IPT Pickup for High-Power Applications. *IEEE Trans. Ind. Electron.* **2010**, *57*, 744–751. [CrossRef]

24. Madawala, U.K.; Thrimawithana, D.J. A Bidirectional Inductive Power Interface for Electric Vehicles in V2G Systems. *IEEE Trans. Ind. Electron.* **2011**, *58*, 4789–4796. [CrossRef]

25. Xia, C.; Chen, R.; Liu, Y.; Chen, G.; Wu, X. LCL/LCC resonant topology of WPT system for constant current, stable frequency and high-quality power transmission. In Proceedings of the 2016 IEEE PELS Workshop on Emerging Technologies: Wireless Power Transfer (WoW), Knoxville, TN, USA, 4–6 October 2016; pp. 110–113. [CrossRef]

26. Thrimawithana, D.J.; Madawala, U.K. A Generalized Steady-State Model for Bidirectional IPT Systems. *IEEE Trans. Power Electron.* **2013**, *28*, 4681–4689. [CrossRef]

27. Li, S.; Li, W.; Deng, J.; Nguyen, T.D.; Mi, C.C. A Double-Sided LCC Compensation Network and Its Tuning Method for Wireless Power Transfer. *IEEE Trans. Veh. Technol.* **2015**, *64*, 2261–2273. [CrossRef]

28. Varikkottil, S.; Febin Daya, J.L. High-gain LCL architecture based IPT system for wireless charging of EV. *IET Power Electron.* **2019**, *12*, 195–203. [CrossRef]

29. Yan, Z.; Zhang, Y.; Song, B.; Zhang, K.; Kan, T.; Mi, C. An LCC-P Compensated Wireless Power Transfer System with a Constant Current Output and Reduced Receiver Size. *Energies* **2019**, *12*, 172. [CrossRef]

30. Chen, Y.; Zhang, H.; Park, S.J.; Kim, D.H. A Comparative Study of S-S and LCCL-S Compensation Topologies in Inductive Power Transfer Systems for Electric Vehicles. *Energies* **2019**, *12*, 1913. [CrossRef]

31. Ann, S.; Lee, W.Y.; Choe, G.Y.; Lee, B.K. Integrated Control Strategy for Inductive Power Transfer Systems with Primary-Side LCC Network for Load-Average Efficiency Improvement. *Energies* **2019**, *12*, 312. [CrossRef]

32. Geng, Y.; Li, B.; Yang, Z.; Lin, F.; Sun, H. A High Efficiency Charging Strategy for a Supercapacitor Using a Wireless Power Transfer System Based on Inductor/Capacitor/Capacitor (LCC) Compensation Topology. *Energies* **2017**, *10*, 135. [CrossRef]

33. Ramezani, A.; Farhangi, S.; Iman-Eini, H.; Farhangi, B.; Rahimi, R.; Moradi, G.R. Optimized LCC-Series Compensated Resonant Network for Stationary Wireless EV Chargers. *IEEE Trans. Ind. Electron.* **2019**, *66*, 2756–2765. [CrossRef]

34. Zhang, Y.; Yan, Z.; Kan, T.; Liu, Y.; Mi, C.C. Modelling and analysis of the distortion of strongly-coupled wireless power transfer systems with SS and LCC–LCC compensations. *IET Power Electron.* **2019**, *12*, 1321–1328. [CrossRef]

35. Mohamed, A.A.S.; Berzoy, A.; de Almeida, F.G.N.; Mohammed, O. Modeling and Assessment Analysis of Various Compensation Topologies in Bidirectional IWPT System for EV Applications. *IEEE Trans. Ind. Appl.* **2017**, *53*, 4973–4984. [CrossRef]

36. Lu, F.; Hofmann, H.; Deng, J.; Mi, C. Output power and efficiency sensitivity to circuit parameter variations in double-sided LCC-compensated wireless power transfer system. In Proceedings of the 2015 IEEE Applied Power Electronics Conference and Exposition (APEC), Charlotte, NC, USA, 15–19 March 2015; pp. 597–601. [CrossRef]

37. Lu, S.; Deng, X.; Shu, W.; Wei, X.; Li, S. A New ZVS Tuning Method for Double-Sided LCC Compensated Wireless Power Transfer System. *Energies* **2018**, *11*, 307. [CrossRef]

38. Hart, D.W. *Power Electronics*; Tata McGraw-Hill Education: New York, NY, USA, 2011.

39. Li, Z.; Zhu, C.; Jiang, J.; Song, K.; Wei, G. A 3-kW Wireless Power Transfer System for Sightseeing Car Supercapacitor Charge. *IEEE Trans. Power Electron.* **2017**, *32*, 3301–3316. [CrossRef]

40. Vázquez, J.; Roncero-Sánchez, P.; Parreño Torres, A. Simulation Model of a 2-kW IPT Charger with Phase-Shift Control: Validation through the Tuning of the Coupling Factor. *Electronics* **2018**, *7*, 255. [CrossRef]

41. Dehui, W.; Qisheng, S.; Xiaohong, W.; Fan, Y. Analytical model of mutual coupling between rectangular spiral coils with lateral misalignment for wireless power applications. *IET Power Electron.* **2018**, *11*, 781–786. [CrossRef]

42. López-Alcolea, F.J.; d. Real, J.V.; Roncero-Sánchez, P.; Torres, A.P. Modeling of a Magnetic Coupler Based on Single- and Double-Layered Rectangular Planar Coils With In-Plane Misalignment for Wireless Power Transfer. *IEEE Trans. Power Electron.* **2020**, *35*, 5102–5121. [CrossRef]

43. del Toro García, X.; Vázquez, J.; Roncero-Sánchez, P. Design, implementation issues and performance of an inductive power transfer system for electric vehicle chargers with series–series compensation. *IET Power Electron.* **2015**, *8*, 1920–1930. [CrossRef]

44. Kan, T.; Nguyen, T.; White, J.C.; Malhan, R.K.; Mi, C.C. A New Integration Method for an Electric Vehicle Wireless Charging System Using LCC Compensation Topology: Analysis and Design. *IEEE Trans. Power Electron.* **2017**, *32*, 1638–1650. [CrossRef]

45. Kan, T.; Lu, F.; Nguyen, T.; Mercier, P.P.; Mi, C.C. Integrated Coil Design for EV Wireless Charging Systems Using LCC Compensation Topology. *IEEE Trans. Power Electron.* **2018**, *33*, 9231–9241. [CrossRef]

46. Liu, C.; Ge, S.; Guo, Y.; Li, H.; Cai, G. Double-LCL resonant compensation network for electric vehicles wireless power transfer: Experimental study and analysis. *IET Power Electron.* **2016**, *9*, 2262–2270. [CrossRef]

47. Liu, X.; Clare, L.; Yuan, X.; Wang, C.; Liu, J. A Design Method for Making an LCC Compensation Two-Coil Wireless Power Transfer System More Energy Efficient Than an SS Counterpart. *Energies* **2017**, *10*, 1346. [CrossRef]

48. Scott, D.W. *Multivariate Density Estimation: Theory, Practice, and Visualization*; John Wiley & Sons: Hoboken, NJ, USA, 2015.